Geochimica et Cosmochimica Acta 343 (2023) 353–370

Contents lists available at ScienceDirect

Geochimica et Cosmochimica Acta

journal homepage: www.elsevier.com/locate/gca

Sulfate and phosphate oxyanions alter B/Ca and $\delta^{11}B$ in inorganic calcite at constant pH: Crystallographic controls outweigh normal kinetic effects

Joji Uchikawa [a,*], Donald E. Penman [b,1], Dustin T. Harper [c,2], Jesse R. Farmer [d,e], James C. Zachos [c], Noah J. Planavsky [b], Richard E. Zeebe [a]

[a] Department of Oceanography, SOEST, University of Hawaii at Manoa, United States
[b] Department of Geology and Geophysics, Yale University, United States
[c] Department of Earth and Planetary Sciences, University of California Santa Cruz, United States
[d] Department of Geosciences, Princeton University, United States
[e] Department of Climate Geochemistry, Max Planck Institute for Chemistry, Germany

ARTICLE INFO

Article history:
Received 25 June 2022
Accepted 12 December 2022
Available online 17 December 2022
Associate editor: Claire Rollion-Bard

Keywords:
Boron paleo-proxies
B/Ca
$\delta^{11}B$
Inorganic carbonate precipitation experiments
Sulfate

ABSTRACT

We report new results from inorganic experiments in which the effects of several oxyanions on the concentration and isotopic composition of boron (B/Ca and $\delta^{11}B$, respectively) in calcite were explored. The oxyanions examined here (sulfate, phosphate, nitrate, and nitrite) differ in their size, charge, and geometric configuration, but they are all common dissolved constituents in natural aqueous solutions including seawater. Of those, sulfate and phosphate which are known to inhibit calcite nucleation/precipitation had pronounced impacts on the B incorporation and isotope fractionation during calcite precipitation. Additions of up to 5 mmol sulfate and up to 2 μmol phosphate into experimental solutions of otherwise unaltered condition caused comparable declines in calcite precipitation rates *R*, increases in B/Ca, and decreases in calcite $\delta^{11}B$ towards the calculated $\delta^{11}B$ of $B(OH)_4^-$. The pattern of changes in B/Ca and $\delta^{11}B$ as a function of *R* observed here is at odds with normal kinetic effects confirmed in previous studies, where B/Ca and $\delta^{11}B$ were shown to increase and decrease, respectively, with an increase in degrees of calcite saturation in solutions and thus *R*. We argue that the paradoxical and apparently reversed kinetic trends in B/Ca and $\delta^{11}B$ in the presence of sulfate and phosphate can be attributed to deformations of the calcite lattice structure due to their substitutions for lattice CO_3, which in turn enhances the retainment and eventual incorporation of $B(OH)_4^-$. Our new findings could have important implications for paleo-reconstructions of ocean carbonate chemistry using B/Ca and $\delta^{11}B$, if the mechanism proposed above is similarly in effect during natural precipitation of biogenic calcite (*e.g.*, foraminiferal tests) in seawater. Though this needs further testing, if true, the gradual but sizable increase in seawater sulfate over the Cenozoic could have biased foraminiferal B/Ca and $\delta^{11}B$. Our experimental data additionally indicate that Na^+ has the capability of providing charge compensations for substitutions of CO_3 by $B(OH)_4^-$. However, our data also demonstrate that changes in Na^+ concentration do not control the degrees of B incorporation.

1. Introduction

Precipitation of $CaCO_3$ minerals such as calcite plays a crucial role in the global carbon cycle. The mineral precipitation often occurs as a result of biomineralization but it can also occur inorganically in certain settings. Irrespective of whether they form biologically or inorganically, the resultant precipitates in nature rarely represent pure $CaCO_3$ and they contain non-constituent elements (which we collectively refer to as "*E*") at minor/trace concentrations. As the degrees of incorporation of *E* often depend on

* Corresponding author at: Department of Oceanography, University of Hawaii at Manoa, Marine Science Building, #508, 1000 Pope Rd., Honolulu, HI 96822, United States.
E-mail address: uchikawa@hawaii.edu (J. Uchikawa).
[1] Currently at Department of Geosciences, Utah State University, United States.
[2] Currently at Department of Geology and Geophysics, University of Utah, United States.

https://doi.org/10.1016/j.gca.2022.12.018
0016-7037/

physicochemical state of aqueous solutions in which precipitation takes place, *E* concentrations in calcareous fossils or other deposits (measured as *E*/Ca ratios) and their isotopic signatures offer valuable information to study the geochemical, climatic, and environmental history of the Earth (Calvert and Pedersen, 2007; Katz et al., 2010).

Our current understanding of the controls on and degrees of *E* incorporation and fractionations of their stable isotopes during $CaCO_3$ precipitation owe to a wealth of prior experimental studies in which $CaCO_3$ was inorganically precipitated under well-controlled conditions (*e.g.*, see the list in Rimstidt et al., 1998). While these studies offer valuable insights into the effect of some key physicochemical parameters (temperature, pH, $CaCO_3$ saturation state, *etc.*) on *E*/Ca, what has been largely overlooked until recently is the potential ancillary influence or biases caused by other dissolved constituents that may be present in experimental and natural solutions. This can be an important consideration when comparing data from independent studies that differ in the choice of experimental solutions and when those observations are extrapolated to natural $CaCO_3$ formed in complex solutions (seawater, organismal fluids, cave drip water, *etc.*). In theory, a given ionic species could hinder incorporation of *E* of interest by posing a direct competition for binding sites or promote incorporation by resolving charge imbalances for altervalent substitutions in $CaCO_3$ (Hellebrandt et al., 2016) and/or by altering the crystallinity of $CaCO_3$ (Mucci and Morse, 1983; Busenberg and Plummer, 1985; Goetschl et al., 2019). Another important consideration is ionic interactions (*e.g.*, formations of ion-pairs) that can influence the activity of ionic forms of *E* as well as Ca^{2+} and CO_3^{2-} ions. These changes may impose additional kinetic controls on *E* incorporation by modulating $CaCO_3$ precipitation rates.

Here, we explore if and how certain oxyanions influence the degrees and processes of boron (B) incorporation into inorganic calcite. Both B concentration and isotopic composition in $CaCO_3$ (B/Ca and $\delta^{11}B$, respectively) are well-recognized as proxies for past changes in ocean carbonate chemistry and pH (Foster and Rae, 2016; Hönisch et al., 2019). But there are still some unsettled caveats in the theoretical basis upon which the B proxies were initially conceptualized and since developed. The motivation for this work builds on preliminary indications that B incorporation into inorganic calcite may be influenced by the presence of SO_4^{2-} in solutions (Uchikawa et al., 2017). This may have important implications for the boron paleo-proxies because SO_4^{2-} is a major ionic constituent of seawater and its concentration in seawater has changed sizably in the past (about two-folds increase over the Cenozoic: Horita et al., 2002; Lowenstein et al., 2003; Brennan et al., 2013; Algeo et al., 2015; Zeebe and Tyrrell, 2019). Here, we explored how changes in concentration of SO_4^{2-} and additionally three other oxyanions (HPO_4^{2-}, NO_3^- and NO_2^-) would influence B/Ca and $\delta^{11}B$ of inorganically precipitated calcite.

2. The boron paleo-proxies

B/Ca and $\delta^{11}B$ paleo-proxies are grounded in sound chemical principles, unlike some other proxies that are based on simple empirical observations. This, in theory, provides greater confidence in interpreting B/Ca and $\delta^{11}B$ recorded in calcareous fossils. In this section, we briefly summarize how the B proxies have been developed and new findings from recent studies that highlight the complexity in B incorporation processes during $CaCO_3$ precipitation.

Dissolved B in seawater predominantly exists as trigonal $B(OH)_3$ and tetrahedral $B(OH)_4^-$ (B_3 and B_4, hereafter, respectively) and their speciation shifts from B_3 to B_4 with an increase in pH. Combined with the constancy in $\delta^{11}B$ of the total seawater B (Foster et al., 2010) and isotope fractionation between B_3 and B_4 (Kakihana et al., 1977; Klochko et al., 2006; Nir et al., 2015), this pH-driven speciation also causes their $\delta^{11}B$ values to change predictably with pH. By examining B concentrations and $\delta^{11}B$ values of modern marine carbonates, Hemming and Hanson (1992) argued that B_4 is selectively incorporated into $CaCO_3$ minerals over B_3 with negligible isotope fractionation as:

$$CaCO_3 + B(OH)_4^- \rightarrow Ca(HBO_3) + HCO_3^- + H_2O \quad (1)$$

Equation-1 implies tetrahedral to trigonal coordination change for B during incorporation into $CaCO_3$. This model gained support from two subsequent studies, where $\delta^{11}B$ of inorganic $CaCO_3$ closely agreed with those of B_4 at precipitation pH (Hemming et al., 1995; Sanyal et al., 2000), albeit this was based on now outdated isotope fractionation factor between B_3 and B_4 ($^{11}\alpha_{B3\text{-}B4}$) by Kakihana et al. (1977). This framework implies that $\delta^{11}B$ measured on marine carbonates can be translated to seawater pH (as reviewed and summarized in Foster and Rae, 2016; Hönisch et al., 2019). Moreover, Eq. (1) intuitively points to a causal relationship between B/Ca of $CaCO_3$ and pH-driven B speciation (with more B incorporated into $CaCO_3$ at higher $[B_4]$). This makes B/Ca a useful complement to $\delta^{11}B$ in studying past changes in ocean carbonate chemistry (*e.g.*, Penman et al., 2014; Harper et al., 2020).

However, more recent experimental and theoretical studies now provide nuanced views of B incorporation, particularly in inorganic $CaCO_3$ precipitated from laboratory experiments. Those include (**#1**) polymorphic and/or crystallographic differences in the degrees of B incorporation (Mavromatis et al., 2015, 2021; Noireaux et al., 2015; Evans et al., 2020; Henehan et al., 2022), (**#2**) apparent $CaCO_3$ growth rate (*i.e.*, kinetic) effects on B incorporation (Gabitov et al., 2014; Mavromatis et al., 2015; Uchikawa et al., 2015, 2017; Kaczmarek et al., 2016; Holcomb et al., 2016; Henehan et al., 2022), (**#3**) the occurrence both tetrahedral and trigonal form of B in calcite as opposed to the dominance of tetrahedral B in aragonite (Mavromatis et al., 2015; Noireaux et al., 2015), (**#4**) a few permil (‰) of positive $\delta^{11}B$ offsets in calcite relative to aqueous B_4 (Farmer et al., 2019; Noireaux et al., 2015; Henehan et al., 2022) based on the revised $^{11}\alpha_{B3\text{-}B4}$ (Klochko et al., 2006; Nir et al., 2015), (**#5**) variable (but up to over 10 ‰) potential equilibrium isotope fractionation between $CaCO_3$-hosted or surface-adsorbed B relative to aqueous B_4 (Balan et al., 2018; Saldi et al., 2018), and (**#6**) the presence of B as both structural and non-structural component in $CaCO_3$ (Balan et al., 2016). Thus, especially in case of calcite, the process of B incorporation is more complicated than previously thought (Eq. (1)).

In our previous studies (Uchikawa et al., 2015; 2017), we conducted calcite precipitation experiments by systematically varying solution carbonate chemistry and some other parameters. We found that, both in relatively dilute $CaCl_2$-Na_2CO_3-NaCl-B solutions (Uchikawa et al., 2015) and in Mg-free artificial seawater (Uchikawa et al., 2017), the primary controls on B/Ca in inorganic calcite are precipitation rates "*R*" and the concentration ratio of the sum of dissolved B and inorganic carbon species ($[B_{Total}]$/[DIC], where $[B_{Total}] = [B_3] + [B_4]$ and $[DIC] \approx [HCO_3^-] + [CO_3^{2-}]$ for the experimental pH range), as opposed to the $[B_4]/[HCO_3^-]$ ratio (as Eq. (1) would imply). Farmer et al. (2016; 2019) later found that $\delta^{11}B$ values of the samples from Uchikawa et al. (2015) are all higher than the expected $\delta^{11}B$ of B_4 in their experimental solutions. These findings call for additional B incorporation pathways involving B_3, for which non-structural sites or defects in the calcite lattice may be important (Hemming et al., 1998; Ruiz-Agudo et al., 2012; Uchikawa et al., 2015; 2017; Balan et al., 2016). However, the ^{11}B enrichments in the calcite samples relative to B_4 found by Farmer et al. (2016; 2019) were typically within 4 to 6 ‰, despite $\delta^{11}B$ of B_3 being higher than B_4 by ≥ 26 ‰ (Klochko et al., 2006; Nir et al., 2015). This still conforms B in calcite to be mainly derived from aqueous B_4 (Hemming et al., 1995).

In Uchikawa et al. (2017), we also tested the effect of (**#1**) Na_2HPO_4 additions to the Mg-free artificial seawater and (**#2**) elevating salinity, after Henehan et al. (2015) and Allen et al. (2011; 2012). While both treatments resulted in a decrease in *R*, they surprisingly enhanced B incorporation. One common consequence for these treatments was the increase in oxyanion concentration in the experimental solutions (HPO_4^{2-} for #1 and SO_4^{2-} for #2). This led us to propose that, besides the primary control by *R* and the $[B_{Total}]/[DIC]$ ratio, certain oxyanions in solution may exert an ancillary control on B incorporation. Moreover, despite the similarity in solution $[B_{Total}]$ and the range of *R*, B incorporation was consistently higher in our 2017 study than in our 2015 study (see Fig. 5 in Uchikawa et al., 2017). This could be ascribed to SO_4^{2-}, as its presence was the primary difference in the solution matrix used in Uchikawa et al. (2015) versus Uchikawa et al. (2017).

In this work, we revisited this hypothesis with the aim of examining whether and to what extent SO_4^{2-} influences the processes of B incorporation into calcite. We also examined the influence of HPO_4^{2-}, NO_3^- and NO_2^- due to their occurrence and biogeochemical importance. For instance, they are essential nutrients for photosynthetic organisms including algal symbionts in association with certain groups of marine calcifiers. The oxyanions tested here vary in mass, size, charge, and geometric configuration (Table 1).

3. Methods

3.1. Overview of the inorganic calcite precipitation experiments

Our inorganic calcite precipitation experiments followed the approach by Uchikawa et al. (2015; 2017), where precipitation occurred in the form of overgrowth onto calcite seeds in 1 L of solutions at 25 °C. In order to highlight the effect of the oxyanions, we chose simple $CaCl_2$-Na_2CO_3-B solutions as the baseline for our experiments. Then several oxyanions were added to this baseline in variable amounts as Na-based salts. The experimental solutions were prepared by dissolving $B(OH)_3$ and oxyanion salts in N_2-bubbled (*i.e.*, $CO_{2(aq)}$-free) MilliQ deionized H_2O preadjusted to 25 °C and volumetrically adding $CaCl_2$. Solution [DIC] was brought to desired levels by adding 0.3 M ^{13}C-spiked Na_2CO_3 solution, along with small volumes of HCl for pH adjustments. After bringing the final volume to 1 L with the same deionized H_2O, the solution was first titrated with 0.3 M NaOH to reach the target pH (pH_{NBS} = ~8.11 and ~8.20: see Section 3.2) and then equilibrated for 1.5 h thereafter. The experimental solutions used in this study were oversaturated with respect to calcite, but not to the extent where precipitation would start spontaneously. In fact, solution pH remained steady during the equilibration period (*e.g.*, see Fig. 3A in Uchikawa et al., 2015). The titrant was then switched to the 0.3 M ^{13}C-spiked Na_2CO_3 solution and calcite seeds were introduced to trigger $CaCO_3$ precipitation, which was easily identifiable by steady pH decline (see Zeebe and Sanyal, 2002; Uchikawa et al., 2015). Once sufficient mass of new calcite as the overgrowth was formed, experiments were terminated and the resultant samples (=seeds + overgrowth) were filtered, rinsed with deionized H_2O, and dried in a 65 °C oven overnight.

The seeds used in our experiments were devoid of the elements considered here (B, P, S and Na) and homogeneous in $\delta^{13}C$ ($\delta^{13}C_{VPDB}$ = −18.07 ± 0.03 ‰, ± 1σ SD, *n* = 5). Based on this and the ^{13}C-spike applied to the Na_2CO_3 solutions used as the DIC source for our experimental solutions and as the titrant, we performed $\delta^{13}C$ mass balance calculations to constrain the overgrowth fraction in the samples (also see Section 3.5). Upon preparation of each batch of the ^{13}C-spiked Na_2CO_3 solutions, small aliquots were quantitatively precipitated as $BaCO_3$ (following Uchikawa and Zeebe, 2013) as the record of the extent of ^{13}C-spike. The $BaCO_3$ samples were later analyzed for their $\delta^{13}C$ values, from which we defined the expected $\delta^{13}C$ of the calcite overgrowth.

3.2. Experimental design

During the first phase of our study from May 2017 to June 2018 (Phase-1 experiments), the control experiments were set at $[B_{Total}]$ = 0.84 mM, $[Ca^{2+}]$ = 5.00 mM, [DIC] = 2.25 mM and pH_{NBS} = ~8.1. To this baseline, different amounts of Na_2SO_4, Na_2HPO_4, Na_2NO_3 or $NaNO_3$ were individually added with no further changes in solution chemistry. We also performed a set of cross experiments that received comparative additions of 5 mmol of Na_2SO_4, 5 mmol of K_2SO_4 and 10 mmol of NaCl. These cross experiments were designed to verify if the experimental results were driven by SO_4^{2-}, rather than Na^+ liberated from the salts. The experiments were performed with 70 mg of seeds and they were run until roughly 70 mg of overgrowth was formed. The samples were examined by Scanning Electron Microscope (SEM) and X-ray powder diffraction (XRD) for their surface characteristics and mineralogy and analyzed for B/Ca ratios by inductively coupled plasma mass spectrometers (ICPMS).

The second phase of the study (Phase-2 experiments) from October 2018 to January 2019 focused only on Na_2SO_4 and Na_2HPO_4, and the samples were analyzed more holistically for B/Ca, S/Ca, P/Ca, and Na/Ca as well as for $\delta^{11}B$. To secure sufficient B in our samples for reliable $\delta^{11}B$ measurements, based on the findings from our previous work (Uchikawa et al., 2015; 2017), the experiments were performed at higher $[B_{Total}]$ and calcite saturation ($[B_{Total}]$ = 1.68 mM, $[Ca^{2+}]$ = 5.40 mM, [DIC] = 2.40 mM and pH_{NBS} = ~8.20). Various amounts of Na_2SO_4 and Na_2HPO_4 were added to this baseline. We also repeated two cross experiments with additions of 5 mmol of Na_2SO_4 versus 10 mmol of NaCl. The Phase-2 experiments were performed with 50 mg of seeds and continued until roughly 85 mg of mass gain.

3.3. Solution chemistry modeling

We used the PHREEQC program (Parkhurst and Appelo, 2013) to model the speciation of solutes and saturation of relevant minerals in our experimental solutions. The MINTEQ.v4 thermodynamic database (Ball and Nordstrom, 1991) was used due to its appropriateness for solutions with low ionic strength and its capability to consider all oxyanions tested here. However, it must be warned that PHREEQC outputs can vary significantly if other datasets available in the program are used. Degrees of mineral saturation are measured as saturation index in PHREEQC:

$$\text{Saturation Index} = \log_{10}(Q/K_{SP}) \quad (2)$$

where *Q* is the ion activity product for the constituent ions (*e.g.*, $\{Ca^{2+}\}\cdot\{CO_3^{2-}\}$ for $CaCO_3$ minerals) and K_{SP} is the mineral-specific thermodynamic solubility product. Activities of free ions and ion-pairs are calculated based on the Davies equation in PHREEQC. We also manually constrained the saturation index for amorphous $CaCO_3$ (ACC) and amorphous calcium phosphate (ACP). The K_{SP} for ACC (pK_{SP} = 6.393 at 25 °C) was taken from Brečević and Nielsen (1989), and we used the average of all values compiled in Combes and Rey (2010) as pK_{SP} for ACP (pK_{SP} = 25.675).

For the Phase-2 experiments, we performed additional solution chemistry modeling with the PITZER ion-ion interaction database (Plummer et al., 1988) in PHREEQC following the recommendation by Farmer et al. (2019) for interpretation of B isotope data. The PITZER database only explicitly considers Ca-B_4 ion-pairs for speciation of dissolved B species. This means that the inclusions of oxyanion salts do not alter the B speciation in our calculations, as ion-ion interactions between B_4 and oxyanions and Na^+ have not been determined. Despite this drawback, however, the use of

Table 1
Physical characteristics of the ionic/dissolved species concerned in this study. Estimations of the bond lengths and atomic distances between two neighboring oxygens in the considered oxyanion species were done using the Avogadro molecular editing/visualization software (https://avogadro.cc). The dissolved species were configured as free ions using the program's auto-optimization tool with the UFF force field. Calcite crystallography data available in the Avogadro program was used for the estimates on CO_3 in the calcite lattice. Also shown is the geometric information for HBO_3, which is thought to be the form of B that replaces CO_3 in $CaCO_3$ in the model by Hemming and Hanson (1992: see Eq. (1)) (although modeled as HBO_3^{2-} ion here). 1 Å = 10^{-10} m.

	Molar Mass (g/mol)	Geometric Configuration	*X*—O Bond Length† (Å)	*X*=O Bond Length‡ (Å)	O—O Distances (Å)
CO_3	60.01	Trigonal Planar	1.248	N/A	2.162
HBO_3	59.82	Trigonal Planar	1.460 to 1.463	N/A	2.526 to 2.541
$B(OH)_3$	61.84	Trigonal Planar	1.460	N/A	2.528
$B(OH)_4^-$	78.84	Tetrahedral	1.469	N/A	2.399
NO_2^-	46.01	2D Bent Rod	1.314	1.193	2.172
NO_3^-	62.01	Trigonal Planar	1.314	1.193	2.172 to 2.277*
SO_4^{2-}	96.07	Tetrahedral	1.716	1.536	2.428 to 2.897*
HPO_4^{2-}	95.98	Tetrahedral	1.735 to 1.736	1.552	2.643 to 2.876*
PO_4^{3-}	94.97	Tetrahedral	1.735	1.552	2.649 to 2.871*

† : Length of single bonds between the central atom of C, B, N, S or P and oxygen atoms.
‡ : Length of double bonds between the central atom of C, B, N, S or P and one/some of the oxygen atoms.
* : Atomic distances between two neighboring oxygens can vary if they are singly or doubly bonded with the central atom.

PITZER database facilitates comparison of inorganic B isotope data across a range of solution ionic strength used in different experimental studies (for details, see Farmer et al., 2019). The total B_4 abundance was calculated as the sum of free B_4 and Ca-B_4 complexes. The $\delta^{11}B$ of B_4 was then given by (Zeebe and Wolf-Gladrow, 2001);

$$\delta^{11}B_{B4} = \frac{\delta^{11}B_{Total} * [B_T] - 1000 * \left({}^{11}\alpha_{B3-B4} - 1 \right) * [B_3]}{[B_4] + {}^{11}\alpha_{B3-B4} * [B_3]} \quad (3)$$

where $[B_3]$ and $[B_4]$ were calculated as above, ${}^{11}\alpha_{B3\text{-}B4}$ = 1.026 (Nir et al., 2015), and $\delta^{11}B_{Total}$ = −12.19 ‰ as previously determined in Farmer et al. (2019) for the same $B(OH)_3$ used here and in Uchikawa et al. (2015).

3.4. Geochemical analyses

3.4.1. $\delta^{13}C$ measurement on carbonate samples

All carbonate materials (Phase-1 and Phase-2 inorganic calcite samples, calcite seeds, and $BaCO_3$ samples quantitatively precipitated from the ^{13}C-spiked Na_2CO_3 solutions upon their preparation) were analyzed for $\delta^{13}C$ at the University of California Santa Cruz (UCSC), using a ThermoFinnegan MAT 253 dual-inlet isotope ratio mass spectrometer coupled to a Kiel IV carbonate device. About 60 μg of samples were reacted with orthophosphoric acid (specific gravity = 1.92 g/cm^3) at 75 °C. During each analytical session, in-house carbonate working standard was analyzed for drift correction. The NBS-18 reference material was also analyzed to monitor quality control and long-term performance. As detailed in Uchikawa et al. (2015), reproducibility of $\delta^{13}C$ measurements was significantly poorer on our ^{13}C-enriched samples ($\delta^{13}C_{VPDB}$ = ~200 ‰ for the calcite samples) than on natural carbonates ($\delta^{13}C$ = ~0‰) due to the extreme differences in $\delta^{13}C$ values between our samples and the calibration standards. For instance, ±1σ SD of duplicate $\delta^{13}C$ measurements on the Phase-1 samples was as high as 3.22 ‰ in some cases (but 0.89 ‰ on average) compared to the typical value of ~0.05 ‰ at the UCSC on samples or standards with natural ^{13}C abundances. However, this is tolerable as 3 ‰ of error in $\delta^{13}C$ analysis translates to only 1 % of error in *E*/Ca ratios of the overgrowth fraction in samples after mass balance calculations, which is smaller than the analytical uncertainty for most *E*/Ca measurements.

The $\delta^{13}C$ data for the Phase-1 samples are based on duplicate analyses, with uncertainty given as ±1σ of duplicate measurements on each sample. The data for the Phase-2 samples are mostly based on single measurement. For these, we assigned a constant uncertainty of ±3.22 ‰, which is the largest ±1σ found in the Phase-1 $\delta^{13}C$ dataset.

3.4.2. *E*/Ca measurement on inorganic calcite samples

Calcite samples from the Phase-1 experiments were analyzed for B/Ca ratios at UCSC, by using a Thermo Element XR ICPMS and by following the protocols specially optimized for our inorganic calcite samples (see details in Uchikawa et al., 2015; 2017). About 300 μg of samples were dissolved in 0.075 N Optima grade HNO_3 and analyzed with 4 in-house solution standards prepared to a range of B/Ca ratios using Certi-Prep elemental standards for calibration. The long-term B/Ca precision (±2σ) based on repeat measurements of a consistency standard was better than ±9 % or ±6 μmol/mol. All samples were analyzed in duplicate and the uncertainty is given as ±1σ SD of duplicate measurements, which ranged from ±0.03 to ±1.82 μmol/mol with the average being ±0.58 μmol/mol (or ±3.6 %).

Calcite samples from the Phase-2 experiments were analyzed for *E*/Ca at the Yale Metal Geochemistry and Geochronology Center (YMGGC). Besides B/Ca, we additionally measured S/Ca, P/Ca and Na/Ca for these samples. Sample aliquots were precisely weighed and dissolved in 0.5 M Teflon-distilled HNO_3 adjusted to given a [Ca] of 4 mM. These solutions were then run on a Thermo Element XR ICPMS alongside three in-house standards with a known range of B/Ca, S/Ca, P/Ca and Na/Ca at the same [Ca] of 4 mM. An additional in-house standard was used for drift correction in each analytical session. The long-term precision for routine B/Ca measurements given as ±1σ SD of repeat measurements on the standards is ±6 μmol/mol or ±9 %. The precision for other *E*/Ca during our analytical sessions was ±0.34 mmol/mol or ±11.3 % for S/Ca, ±16.2 μmol/mol or ±10.8 % for P/Ca, and ±0.2 mmol/mol or ±2.5 % for Na/Ca. Since *E*/Ca data for the Phase-2 samples are based on single measurements, we applied the larger of the absolute or % error as the uncertainty.

3.4.3. $\delta^{11}B$ measurement on inorganic calcite samples

A subset of the calcite samples from the Phase-2 experiments were analyzed for $\delta^{11}B$ at the YMGGC. We previously found that B/Ca ratios measured on inorganic calcite samples that were treated with or without several rounds of sonication in B-free MilliQ deionized H_2O fall very close to the 1:1 line (Uchikawa et al., 2015), based on which we omitted sonication steps for our B/Ca measurements. But even trace amounts of surface-adsorbed B (that is too insignificant to obstruct B/Ca within measurement precision) can bias $\delta^{11}B$ measurements. Thus, following Farmer et al. (2019),

we implemented precautionary sonication steps before $\delta^{11}B$ analysis.

About 10 mg of sample aliquots were weighed into acid-cleaned centrifuge tubes and rinsed with B-free MilliQ H_2O, sonicated, and centrifuged 5 times. Samples were then dissolved in 500 mL of 0.5 M Teflon-distilled HNO_3 and a volume of the dissolved sample corresponding to 10 ng of B was used for analysis. B was separated from the $CaCO_3$ matrix by ion chromatography using Amberlite IRA-743 B-specific resin using the methods of Foster (2008) updated by Zhang et al. (2017). Analyses were performed in duplicate for each sample on a Thermo Neptune Plus multi-collector ICPMS with 10^{12} Ω resistors, with each sample bracketed by the NIST 951 reference material. External $\delta^{11}B$ reproducibility (±2σ SD) on the JCp-1 carbonate standard at comparable signal intensity was less than 0.24 ‰ (Zhang et al., 2017).

3.4.4. SEM and XRD

SEM imaging and XRD analyses was performed in the W.M. Keck Cosmochemistry Laboratory and X-ray Atlas Diffraction Laboratory at the University of Hawaii. SEM imaging carried out in October 2022 was by JEOL JSM-5900 LV instrument operating at 15 kV. SEM images were taken after the sample powder was mounted onto adhesive carbon tapes and subsequently gold-sputtered. We used a Bruker D8 Advanced diffractometer (CuKα source operating at 40 mA and 40 kV in a parafocusing Bragg-Brentano mode) with a Lynxeye XE detector for the XRD analyses. A thin layer of each sample powder was placed on a single crystal wafer zero-background plate for the analyses. Search-and-Match mineral phase identification was based on the Bruker Diffrac.Eva software (version 4.2.0.14) with the ICDD PDF 4+ database.

XRD work was done in two separate occasions, March 2018 and October 2022. In 2018, we only analyzed test samples from pilot experiments conducted for the Phase-1 experimental series. During the 2022 XRD session, we analyzed the actual Phase-1 samples (B/Ca of those were measured and reported here) and re-examined one of the test samples analyzed in 2018. For the 2022 XRD results, the width of the most dominant calcite peak at the diffraction angle of ~ 29.5° (d_{104} peak) was quantified as full width at half maximum peak intensity (FWHM):

$$\mathrm{FWHM} = 2 \times \sqrt{ln(2)} \times c_1 \quad (4)$$

where c_1 is a constant that can be obtained by applying a Gaussian fit to the d_{104} peak in XRD profiles using MATLAB's curve-fitting toolbox as:

$$y = a_1 \times exp^{-\left(\frac{x-b_1}{c_1}\right)^2} \quad (5)$$

The d_{104} peak broadening (*i.e.*, increase in FWHM) is considered as a sign of crystallographic imperfection due typically to inclusion of non-constituent elements (*e.g.*, Zhang et al., 2010; Salter et al., 2019).

3.5. Constraining calcite overgrowth and precipitation rate

The quantifications of the overgrowth fraction and their *E*/Ca ratios in inorganic calcite samples were done by the double mass-balance calculations, as detailed in Uchikawa et al. (2015). Analytical uncertainty for both $\delta^{13}C$ and *E*/Ca measurements were propagated through the mass balance calculations. The final error in the calculated *E*/Ca ratios for the overgrowth fraction in samples was mainly due to the error in *E*/Ca measurements. The *E*/Ca values reported and discussed from this point forward are exclusively for the overgrowth fraction.

Calcite precipitation rates *R* exert a major control on elemental and isotopic partitioning of B during $CaCO_3$ precipitation in inorganic systems (Gabitov et al., 2014; Mavromatis et al., 2015; Noireaux et al., 2015; Kaczmarek et al., 2016; Uchikawa et al., 2015, 2017; Farmer et al., 2019). However, constraining *R* can be complicated and often requires some assumptions specific to experimental approaches and conditions, making direct data comparisons across different studies challenging (see Farmer et al., 2019). Since we used the same experimental set-up and the same calcite seeds here, we followed the approach described in Uchikawa et al. (2015) for estimating *R* (in mol/m^2/*sec*). This approach relies on simple geometric and stoichiometric assumptions and approximations to estimate the total surface area provided by the seeds. The reactive surface area should change over time, as the individual seed crystals become larger due to the overgrowth. This means that the estimates made for the beginning and the end of an experiment should provide the upper and lower limit for the area normalized *R*. Our estimates on *R* present the average for the entire experimental duration and the error margins reflect the upper and lower limit described above.

4. Results

4.1. Experimental solution chemistry

As described in Section 3.1 and as fully disclosed in Uchikawa et al. (2015), our pH-stat experimental system is capable of only balancing the changes in pH, [DIC] and alkalinity due to calcite precipitation via titration with (^{13}C-spiked) Na_2CO_3 solution. Inevitable consequences of this are continuous Ca^{2+} drawdown and build-up of Na^+. Based on the overgrowth yields and the records of the Na_2CO_3 titrant concentration and its added volume, it can be estimated that the solution [Ca^{2+}] decreased by roughly 15 % and [Na^+] increased by 10 to 35 % during our experiments (see Table-S1 for details). Estimates for the loss of dissolved B due to uptake into the overgrowth were typically below 0.015 %. Despite the continuous Ca^{2+} drawdown, the rates of titrant addition (≈ $CaCO_3$ precipitation rates) remained steady throughout our experiments. NaCl additions to the baseline control solutions had negligible impact on calcite precipitation kinetics and elemental and isotopic partitioning of B into the overgrowth (see Section 5.1 for more details). It is therefore very unlikely that the excess Na^+ biased our experimental results. Also note that solution chemistry discussed hereafter specifically refers to the initial condition, right before the seed addition to induce calcite precipitation.

The outputs from PHREEQC modeling with the MINTEQ.v4 database for solution chemistry are compiled in Table-S1 in the supplementary material. About 90 % and 8 to 10 % of the total B in solutions was in free un-complexed B_3 and B_4 at the near neutral experimental pH, and Ca-B_4 plus Na-B_4 ion-pairs accounted for less than 1.7 % of the total B in almost all Phase-1 and Phase-2 experiments. As for DIC speciation, over 90 % was accounted for by free HCO_3^-, whereas CO_3^{2-} represented 1.13 % of the total DIC at most. The remaining fraction mainly existed as Ca-HCO_3^+ and Ca-CO_3^0 ion pairs (by about 4 to 5 % and less than 2.75 %, respectively). Over 96 % of Ca existed as free Ca^{2+} ions in most cases. Yet, SO_4^{2-} additions gave rise to Ca-SO_4^0 ion-pairs and reduced the free Ca^{2+} ions, for instance by almost 20 % upon 5 mmol of SO_4^{2-} additions. Of the total phosphates resulted from Na_2HPO_4 additions, roughly 45 %, 35 % and 15 % speciated into free HPO_4^{2-} ions, Ca-HPO_4^0, and Ca-PO_4^- ion-pairs, respectively.

The only mineral phases that were above saturation in all conditions were calcite and aragonite. In case of Na_2HPO_4 addition experiments, however, PHREEQC indicated strong oversaturation with respect to hydroxyapatite (HAP: given as $Ca_5(PO_4)_3OH$). Saturation index (Eq. (2)) for HAP ranged from 6.28 to 8.50, in comparison to 0.96 to 1.10 for calcite. While other thermodynamic

databases gave more conservative HAP saturation index (*e.g.*, 4.26 to 4.67 by the WATEQ4f databases), the degrees of HAP oversaturation were still persistently higher than calcite. Solutions in which 2 μmol of Na_2HPO_4 was added, $Ca_3(PO_4)_2$ were also above saturation. But this mineral should not require further attention, as it is not known to form directly from aqueous solutions at low temperatures (Combes and Rey, 2010; Dorozhkin, 2010). Lastly, solution modeling in conjunction with the K_{SP} by Brečević and Nielsen (1989) and Combes and Rey (2010) indicated undersaturation for ACC and ACP in our experimental solutions.

4.2. Results from the Phase-1 experiments

4.2.1. SEM and XRD data

Fig. 1 shows SEM images of the calcite seeds and select samples from the Phase-1 experiments. The seeds consisted of aggregates of rhombohedral crystals with sharp well-defined edges and smooth surfaces (Fig. 1a). These morphological features were well retained during the control and the $NaNO_3$, $NaNO_2$ and NaCl addition experiments (Fig. 1b and 1e-g). But this was not the case in the Na_2SO_4 and Na_2HPO_4 addition experiments (Fig. 1cd). The samples from the Na_2SO_4 experiment formed additional crystal faces or elongated edges that are apparently angled and notched. With such morphological alteration, the crystals appear out of rhombohedral shape. Although the rhombohedral geometry was better retained in the sample from the Na_2HPO_4 experiment, this sample had notable surface roughness in the form of cavities and crevices.

The XRD results for some of the Phase-1 samples are summarized in Fig. 2. The XRD profiles for the seeds and the control sample show a series of well-resolved peaks indicative of calcite. Calcite was likewise the only identifiable mineral phase in all analyzed samples. Though the XRD profiles were all generally very similar, the sample from the Na_2SO_4 experiment showed a few extra peaks and an apparent change in the overall shape of a peak-cluster at higher diffraction angles (Fig. 2f). Additionally, FWHM of the d_{104} peak for this sample was slightly higher than those for the original seeds and for the sample from the Phase-1 control and $NaNO_3$ experiments (Fig. 2g). The most severe d_{104} peak broadening, however, was found for the sample from the Na_2HPO_4 addition experiment. Also note that the XRD profile for this sample only show the peaks indicative of calcite, despite the strong HAP oversaturation predicted by PHREEQC modeling for all Na_2HPO_4 addition experiments. Formation of HAP in aqueous solution is known to proceed via acid-base transformation of several precursor phases (Brown and Fulmer, 1991; Lazić, 1995; Martin and Brown, 1997). It is plausible that the pH constancy in our experiments prevented HAP formation by blocking some segments of the phase transformation.

Our XRD session in 2018 confirmed no minerals other than calcite in the analyzed test samples from pilot experiments the Phase-1 series (see Fig. S1 in the supplementary material). Yet, aside from the typical calcite peaks, we observed an anomalous broad hump centered around 2θ of ~12° for the test sample from a pilot Na_2HPO_4 experiment. This is a well-known diagnostic feature of non-crystalline phases such as amorphous calcium carbonate (ACC: Blue et al., 2017). However, we were unable to reconfirm this amorphous signal during our re-run of the same sample in 2022. One possibility is that the amorphous signal detected in this sample in 2018 was due to ACC, which gradually transformed into crystalline calcite over time. This is not unrealistic, as our samples were not kept in a desiccator or under vacuum (see Konrad et al., 2016). It should be noted that ACC formation in our experimental conditions is not supported by solution chemistry modelling with K_{SP} from Brečević and Nielsen (1989). But one caveat here is the possible inadequacy of this K_{SP} that was determined in $CaCl_2$-Na_2CO_3 solutions. Factors other than degrees of saturation can influence the formation and stability of ACC, and one such example is the presence of orthophosphate ions in solutions (Zou et al., 2020). Thus, the possibility of ACC cannot be ruled out in our experiments with Na_2HPO_4.

4.2.2. Precipitation kinetics and B/Ca ratios

Fig. 3 provides a visual presentation of the results from the Phase-1 experiments (see Table 2 for numerical data summary and Table-S1 for individual/comprehensive data). The seven replicate runs for the control were quite consistent and reproducible, except for one run that ended up as an apparent B/Ca outlier. Excluding this, precipitation of calcite overgrowth occurred at $\log_{10}R$ of −5.68 ± 0.02 mol/m^2/*sec* with the average B/Ca of 25.84 ± 3.28 μmol/mol (1σ St. Dev., n = 6). Progressive Na_2SO_4 additions up to 5 mmol caused a steady decline in $\log_{10}R$ to −6.19 mol/m^2/*sec*, while B/Ca increased to ~70 μmol/mol at 3 mmol Na_2SO_4 addition and then tapered off. Albeit in considerably lower dosage of only up to 2 μmol, Na_2HPO_4 additions had sizable impacts on both $\log_{10}R$ and B/Ca. While $\log_{10}R$ steadily decreased to −5.88 mol/m^2/*sec*, B/Ca increased to about 90 μmol/mol in response to Na_2HPO_4 additions. In contrast, $NaNO_3$ and $NaNO_2$ additions by up to 3 mmol caused no significant changes in $\log_{10}R$ and B/Ca.

The results from the cross experiments with comparative additions of 5 mmol of Na_2SO_4 and K_2SO_4 versus 10 mmol of NaCl are displayed in Fig. 4. Both Na_2SO_4 and K_2SO_4 addition caused similar degrees of decline in $\log_{10}R$ and increase in B/Ca. But the $\log_{10}R$ and B/Ca from the NaCl experiments were essentially indistinguishable from the control.

4.3. Results from the Phase-2 experiments

The Phase-2 experimental data are summarized in Table 3 and presented in Fig. 5. Calcite precipitation occurred at the average rate of −5.49 ± 0.02 mol/m^2/*sec* for the control, with the average B/Ca and $\delta^{11}B$ being 146.58 ± 6.66 μmol/mol and −29.84 ± 0.15 ‰, respectively. Note also that all our samples had measurable amount of P (average P/Ca of ~25.5 μmol/mol for the whole samples in case of the Phase-2 control) even in experiments without any Na_2HPO_4 additions and despite the lack of residual P in the calcite seeds. The unexpected P likely reflect minor contamination from unknown sources.

While Na_2SO_4 additions by 2 and 5 mmol caused notable reductions in $\log_{10}R$, all E/Ca increased from the control (except P/Ca: see Table 3). At the respective Na_2SO_4 dosage, calcite $\delta^{11}B$ dropped by about 1.9 ‰ and 2.8 ‰ from the control. In contrast, 10 mmol of NaCl addition (a cross experiment paired with 5 mmol of Na_2SO_4 addition) caused negligible changes in $\log_{10}R$, all E/Ca and $\delta^{11}B$ (Fig. 6). Both calcite precipitation kinetics and the extent of B incorporation responded strongly to Na_2HPO_4 additions up to 2 μmol (Fig. 5). The B/Ca increased from the control by a factor of ~ 2, yet $\delta^{11}B$ decreased by about 2 ‰. While Na_2HPO_4 additions had no discernible influence on Na/Ca, they caused an increase in P/Ca by two orders of magnitude.

5. Discussion

5.1. Oxyanions as the driver for the observed experimental results

Each of the Na-based salts differing in their oxyanion constituents had disparate impacts on the experimental outcome. Notice that, when all $\log_{10}R$ and B/Ca data from the relevant experiments are pooled and considered against the amount of Na^+ added in each experiment, no clear and unifying trend exists (Fig. S2). More critically, despite the total Na^+ added being equal, the $\log_{10}R$ and B/Ca results from the comparative Na_2SO_4 and NaCl experi-

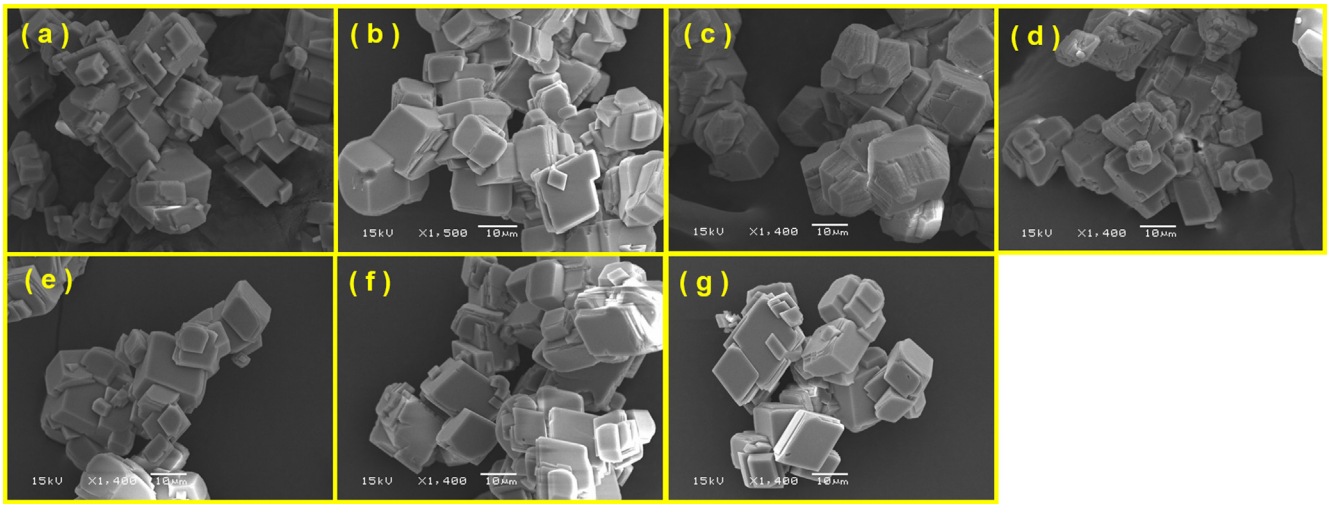

Fig. 1. SEM images of the initial calcite seeds and the samples from the Phase-1 experiments. (a) Initial calcite seeds. (b) Sample "B/Ctr-A" from the control experiment. (c) Sample "B/N-SO4-3A" from the experiment with + 5 mmol of Na_2SO_4. (d) Sample "B/PO4-3A" from the experiment with + 2 µmol of Na_2HPO_4. (e) Sample "B/NO3-1R-A" from the experiment with + 3 mmol of $NaNO_3$. (f) Sample "B/Nitrite-1A" from the experiment with + 3 mmol of $NaNO_2$. (g) Sample "B/NCL-1A" from the experiment with + 10 mmol of NaCl.

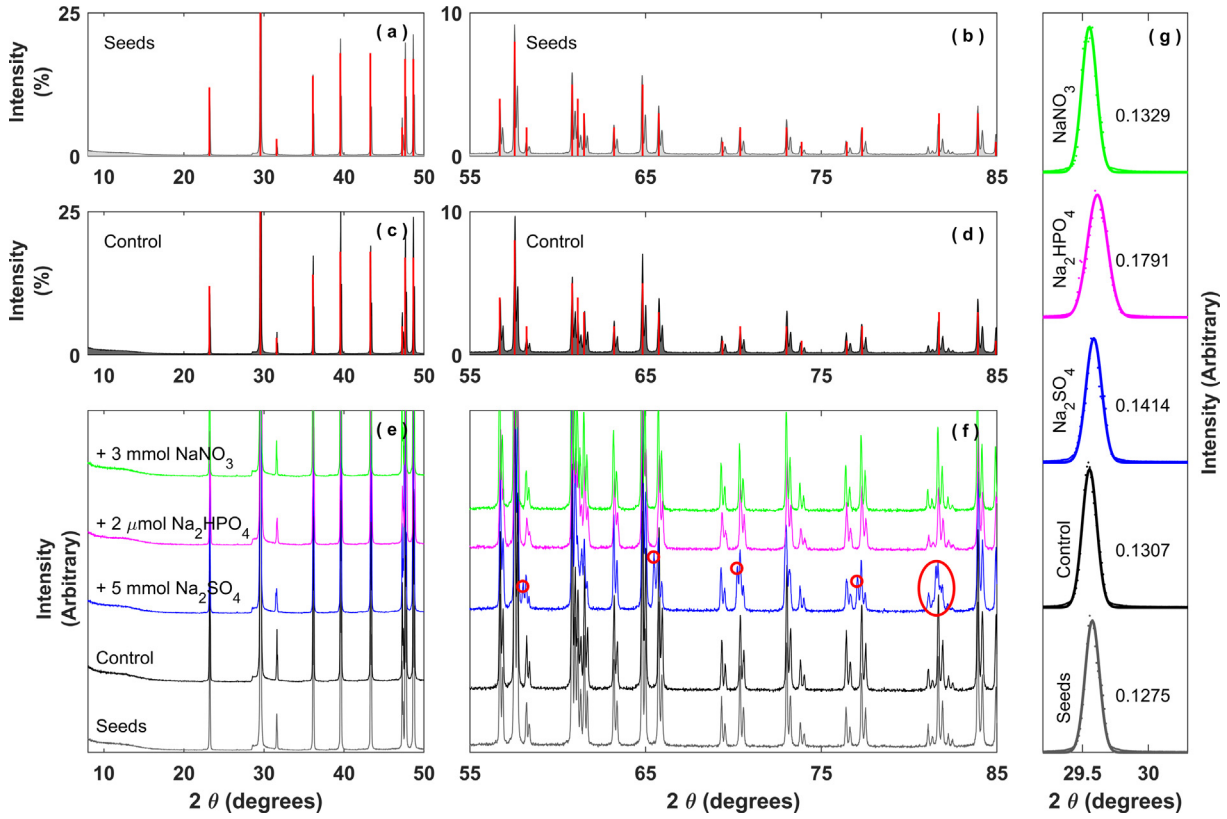

Fig. 2. X-ray diffraction (XRD) pattern of the seeds used in our experiments (panels a and b, gray) and select samples from the Phase-1 experiments (panels c-f) and a comparison of the d_{104} peak broadening (panel g). The middle panels (b, d, and f) provide zoomed views of the peaks at diffraction angles > 55°. XRD counts are normalized to the most dominant d_{104} peak at ~29.5°, such that the d_{104} peak has the relative intensity of 100 %. In panels a-d, XRD profile of the seeds and the Phase-1 control sample is juxtaposed over the reference peaks of calcite shown by red (File 5–586 from the Joint Committee on Powder Diffraction Standards). The XRD pattern for the sample from a Na_2SO_4 addition experiment (blue) is markedly different from the rest, by having extra peaks (small red circle) and a clear change in the overall shape of the stack of peaks around 82° (red ellipse). The numerical values given in the far-right panel (panel g) are FWHM calculated for the d_{104} peak. While the XRD results are shown by the dots, solid curves represent the results of the Gaussian fit to the XRD data for calculating FWHM (Eq-4 and Eq-5). The samples used for these XRD analyses are "B/Ctr-B" for the control (black), "B/N-SO4-3A" for + 5 mmol Na_2SO_4 (blue), "B/PO4-3A" for + 2 µmol Na_2HPO_4 (magenta), and "B/NO3-1R-B" for + 3 mmol $NaNO_3$ (green). See Table S1 for more details about these samples. (For interpretation of the references to color in this figure legend, the reader is referred to the web version of this article.)

Table 2
Summary of the experimental conditions and data from the first phase of the study (Phase-1 experiments). The data shown here are the average and 1σ St. Dev. of the results from replicate experiments at each condition.

Experiment	*n*	$\log_{10}R$ (mol/m²/*sec*)	B/Ca (μmol/mol)
Control	7‡	−5.68 ± 0.02	25.8 ± 3.3
+0.84 mmol Na_2SO_4	3	−5.75 ± 0.01	33.2 ± 1.0
+2 mmol Na_2SO_4	4	−5.84 ± 0.01	37.8 ± 5.5
+3 mmol Na_2SO_4	3	−6.00 ± 0.01	72.1 ± 7.7
+5 mmol Na_2SO_4	3	−6.19 ± 0.01	73.1 ± 5.2
+0.5 μmol Na_2HPO_4	3	−5.74 ± 0.01	52.6 ± 2.7
+1 μmol Na_2HPO_4	4	−5.78 ± 0.01	68.0 ± 5.5
+2 μmol Na_2HPO_4	4	−5.88 ± 0.00	93.6 ± 3.1
+0.1 mmol $NaNO_3$	5	−5.66 ± 0.01	22.3 ± 3.0
+1.5 mmol $NaNO_3$	4	−5.66 ± 0.01	20.4 ± 3.3
+3 mmol $NaNO_3$	5‡	−5.66 ± 0.01	24.8 ± 2.6
+3 mmol $NaNO_2$	4	−5.65 ± 0.02	26.1 ± 5.7
Cross Experiments			
Control	7‡	−5.68 ± 0.02	25.8 ± 3.3
+5 mmol Na_2SO_4	3	−6.19 ± 0.01	73.1 ± 5.2
+5 mmol K_2SO_4	5‡	−6.19 ± 0.01	62.5 ± 1.7
+10 mmol NaCl	5‡	−5.65 ± 0.02	26.2 ± 4.8

‡ : One replicate run resulted in B/Ca outlier. The outlier was not counted for the average $\log_{10}R$ and B/Ca.

ments contradict each other. In the Phase-1 cross experiments, while the Na_2SO_4 additions caused a clear decline in $\log_{10}R$ and an increase in B/Ca, the NaCl additions resulted in no discernible changes in $\log_{10}R$ and B/Ca from the control (Fig. 4). In the Phase-2 cross experiments, the results from the NaCl experiments are likewise no different from the control in terms of *R*, all *E*/Ca and $\delta^{11}B$ (Fig. 6). Lastly, the $\log_{10}R$ and B/Ca results from the Phase-1 cross experiments with 5 mmol of Na_2SO_4 versus K_2SO_4 additions were quite comparable (Fig. 4). These lines of evidence suggest that changes in calcite precipitation kinetics, *E*/Ca and $\delta^{11}B$ must be driven by the oxyanions liberated from the salts, rather than Na^+.

5.2. The normal kinetic effects for B/Ca and $\delta^{11}B$

In our previous studies (Uchikawa et al., 2015; 2017; Farmer et al., 2016; 2019), changes in calcite precipitation rates *R* via pH, [DIC] and [Ca^{2+}] manipulations significantly influenced both B/Ca and $\delta^{11}B$. Specifically, λ_B exponentially increased and $^{11}\varepsilon_{CaCO3\text{-}B4}$ linearly decreased with $\log_{10}R$ (Fig. 7), where λ_B and $^{11}\varepsilon_{CaCO3\text{-}B4}$ are the apparent B partition coefficient (Uchikawa et al., 2015) and ^{11}B enrichment factor in calcite relative to aqueous B_4, respectively:

$$\lambda_B = (B/Ca)_{CaCO3}/([B_{Total}]/[DIC])_{Solution} \quad (6)$$

and

$$^{11}\varepsilon_{CaCO3-B4} = \{(\delta^{11}B_{CaCO3} + 10^3)/(\delta^{11}B_{B4} + 10^3) - 1\}10^3 \quad (7)$$

Farmer et al. (2019) demonstrated that a surface kinetic model adopted from Branson (2018) is capable of simultaneously replicating the overall pattern of changes in λ_B and $^{11}\varepsilon_{CaCO3\text{-}B4}$ as a function of $\log_{10}R$, as long as both B_4 and B_3 were taken into account for incorporation of B. This was proven to be the case for model applications to data from other experimental studies as well (Noireaux et al., 2015; Kaczmarek et al., 2016). The framework of their model considers B incorporation as a competition or balance between the attachment and detachment rates of aqueous B species to/from the calcite surface. As for the attachment, B_4 can be more readily attracted to the calcite surface because of its negative charge (following Hemming et al., 1995, but see Section 5.3 below), while the attachment of uncharged B_3 is assumed to be purely stochastic. But once attached to the surface, B_3 should be less likely to be detached due to its trigonal coordination directly compatible with the configuration of CO_3 in calcite. When calcite grows more slowly (*e.g.*, at lower saturation), B incorporation is largely detachment-driven, as there is more opportunity for B_4 to be detached from the surface before being incorporated. This moderates the overall B incorporation, yet increases the B_3 contribution to the total B incorporated. The end results are lower calcite B/Ca but higher $^{11}\varepsilon_{CaCO3\text{-}B4}$ at lower *R*. Upon rapid growth (*e.g.*, at higher saturation), incorporation is attachment-oriented, as B_4 can be successfully incorporated before being detached. This enhances the overall B incorporation but reduces the B_3 contribution in calcite. At higher *R*, the end results are elevated calcite B/Ca but lower $\delta^{11}B$, such that calcite $\delta^{11}B$ is in closer agreement with B_4. So, when *R* depends only on calcite saturation state (*i.e.*, changes in pH, [DIC] and [Ca^{2+}]) and at a constant solution [B_{Total}], faster precipitation leads to higher B/Ca in calcite but a decline in $^{11}\varepsilon_{CaCO3\text{-}B4}$ towards 0 (Fig. 7). We refer to this pattern as the "normal kinetic effects" for B incorporation.

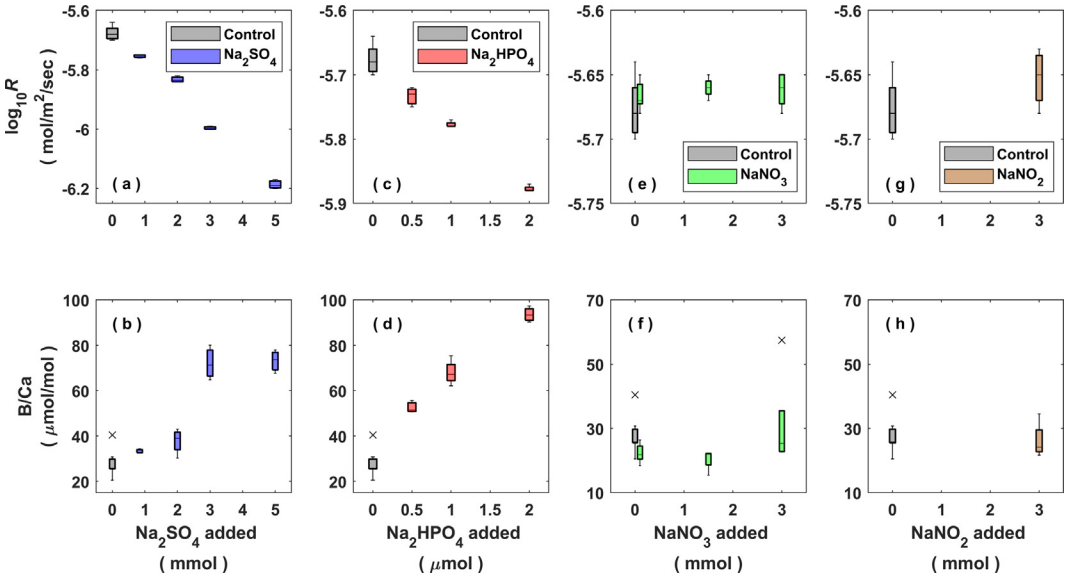

Fig. 3. Observed changes in calcite precipitation rates *R* (upper panels) and B/Ca as a function the amount of Na_2SO_4 (a and b), Na_2HPO_4 (c and d), $NaNO_3$ (e and f) and $NaNO_2$ (g and h) added to the experimental solutions. Data obtained from replicate runs at each experimental condition are compiled and displayed here as whisker plots. B/Ca data points shown by cross symbols are outliers.

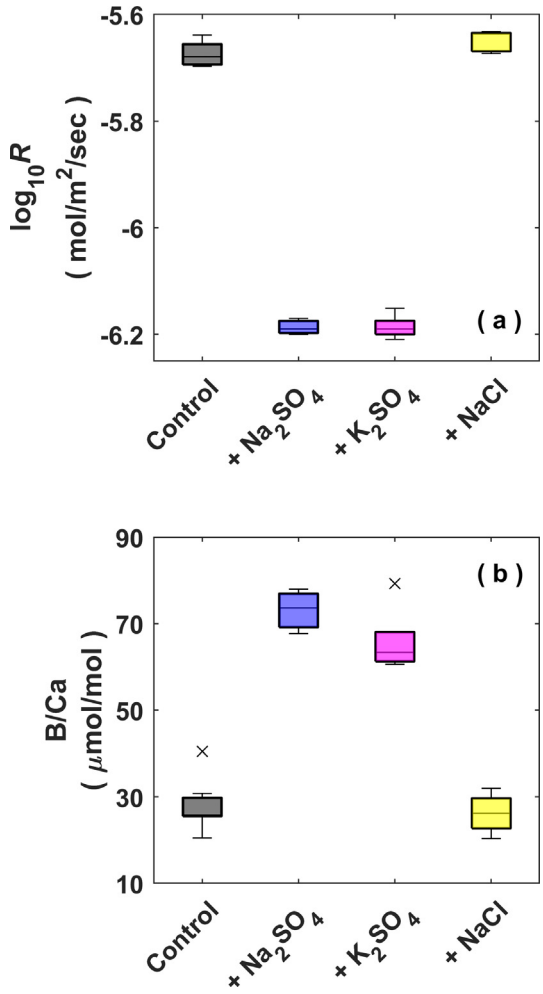

Fig. 4. Summary and comparison of the results from the Phase-1 cross experiments in which 5 mmol of Na_2SO_4, 5 mmol of K_2SO_4 and 10 mmol of NaCl was individually added to the control condition. Cross symbols represent outliers in the B/Ca results. Note that Na_2SO_4 and K_2SO_4 addition resulted in similar degrees of decrease in calcite precipitation rates (a) and increase in B/Ca (b). In contrast, $\log_{10}R$ and B/Ca from the NaCl addition experiment are practically no different from the control.

Our new data portray a pattern that is totally opposite of the normal kinetic effects (Fig. 7), such that λ_B increases and $^{11}\varepsilon_{CaCO3\text{-}B4}$ decreases with *decreasing* $\log_{10}R$, as occurs with further SO_4^{2-} additions. The pattern also holds true for the data from the experiments with Na_2HPO_4 additions (that mostly resulted in free and complexed forms of HPO_4^{2-}: Section 4.1). The steady decline in R caused by SO_4^{2-} and HPO_4^{2-} additions observed here (Figs. 3 and 5) is consistent with the notion that they are both highly effective calcite precipitation inhibitors (Busenberg and Plummer, 1985; Nielsen et al., 2016; Mucci, 1986; Burton and Walter, 1990; Dove and Hochella, 1993; Plant and House, 2002; Lin and Singer, 2005). If the normal kinetic effects are the first-order control (which is seemingly the case in most, if not all, of the prior experimental studies: see Farmer et al., 2019), given no changes in solution $[B_{Total}]/[DIC]$ ratio in our experiments, we would expect a decrease in B/Ca (thus λ_B) and an increase in $\delta^{11}B$ (thus $^{11}\varepsilon_{CaCO3\text{-}B4}$) with a decrease in R as a result of SO_4^{2-} and HPO_4^{2-} additions. But this is clearly not the case (Fig. 7). It follows that B incorporation must be influenced by other unique and crucial processes that are directly or indirectly related to these tetrahedral oxyanions.

The key reference frame for data interpretation and comparison (Fig. 7) is the calcite precipitation rates R. Given the lack of direct surface area BET measurements, we relied on an indirect approach to estimate the total surface area provided by the seeds (Section 3.5: also see Zeebe and Sanyal, 2002; Uchikawa et al., 2015; 2017). Hence, the surface area normalization for our estimates on R bares an intrinsic uncertainty due, for example, to some size heterogeneity in the seeds (Fig. 1a). Crystal surface roughness and irregularities observed for the samples produced in solutions with the presence of SO_4^{2-} and HPO_4^{2-} (Fig. 1cd) represents another source of uncertainty for estimating R. We argue, however, these should neither invalidate the data comparison presented in Fig. 7, refute the robust decline in $\log_{10}R$ caused by SO_4^{2-} and HPO_4^{2-}, nor discredit our overall data interpretations for two reasons. First, the same calcite seeds were used here and previously, without any special pre-treatments. It follows that the intrinsic uncertainty in R between the present and our previous studies (Uchikawa et al., 2015; 2017; Farmer et al., 2019) is more or less internally consistent. Second, the crystal surface roughness (Fig. 1 cd) should translate to an extra surface area (this should also be the case for ACC, if it was involved in HPO_4^{2-} addition experiments: see Section 4.2.1 and Fig. S1). If this is properly quantified and taken into an account for the surface area normalization, our estimates for R for the SO_4^{2-} and HPO_4^{2-} addition experiments should decrease. In other words, the decreasing trends in $\log_{10}R$ as a function of SO_4^{2-} and HPO_4^{2-} additions (Fig. 3 and Fig. 5) are to be more strongly pronounced, which does not invalidate the λ_B and $^{11}\varepsilon_{CaCO3\text{-}B4}$ trends that are opposite of the normal kinetic effects (Fig. 7).

5.3. Possible roles of oxyanions in solutions and near the calcite surface

Differences in ionic strength and/or types and concentrations of background electrolytes in solutions can affect experimental determinations of calcite precipitation kinetics and elemental uptake (*e.g.*, see Fig. 5 in Uchikawa et al., 2017). So, it is possible that our results may be partly due to some changes in ionic interactions in the experimental solutions by the oxyanion additions, but perhaps except for the Na_2HPO_4 experiments where the effect, if any, should be minimal due to the very small additions (at least 3 orders of magnitude less than the other components/salts added to the experimental solutions: see Section 3.2 and Table-S1).

Henehan et al. (2022) recently emphasized the importance of the electric charge across the diffusion boundary layer (DBL) between the $CaCO_3$ surface and the bulk solution. The surface charge carried by $CaCO_3$ (including calcite) is considered positive, which was called upon by Hemming et al. (1995) as one supporting argument for selective incorporation of negatively-charged B_4 over neutral B_3 (Section 2). However, Henehan et al. (2022) challenged this view because, before making the contact to the calcite surface, B_4 must first pass through the DBL in which the charge is claimed to be weakly negative. The landscape of the electric charge in the DBL depends on the types and concentrations of so-called potential determining ions (PDIs), which include most of the ions present in our experimental solutions. While the possibility of NO_3^- and NO_2^- as PDIs is largely unknown (to the best of our knowledge), data from several studies agree that introduction of SO_4^{2-} into solutions renders the charge in the DBL more negative (Zhang and Austad, 2006; Alroudhan et al., 2016; Al Mohrouqi et al., 2017; Song et al., 2017). This makes the situation even more unfavorable for diffusion of negatively-charged B_4 towards the calcite surface. One potentially effective way for B_4 to overcome this hurdle would be to form $CaB(OH)_4^+$ ion-pairs with Ca^{2+} (Henehan et al., 2022). However, SO_4^{2-} readily complexes with Ca^{2+} and forms $CaSO_4^0$ ion-pairs in solutions (Kester and Pytkowicz, 1969; Ball and Nordstrom, 1991). In fact, PHREEQC modeling shows a decrease in $CaB(OH)_4^+$ ion-pairs in response to progressive SO_4^{2-} additions into experimental solutions due to the formation of Ca-SO_4^0 ion-pairs (Table-S1). Thus, raising solution $[SO_4^{2-}]$ should work against

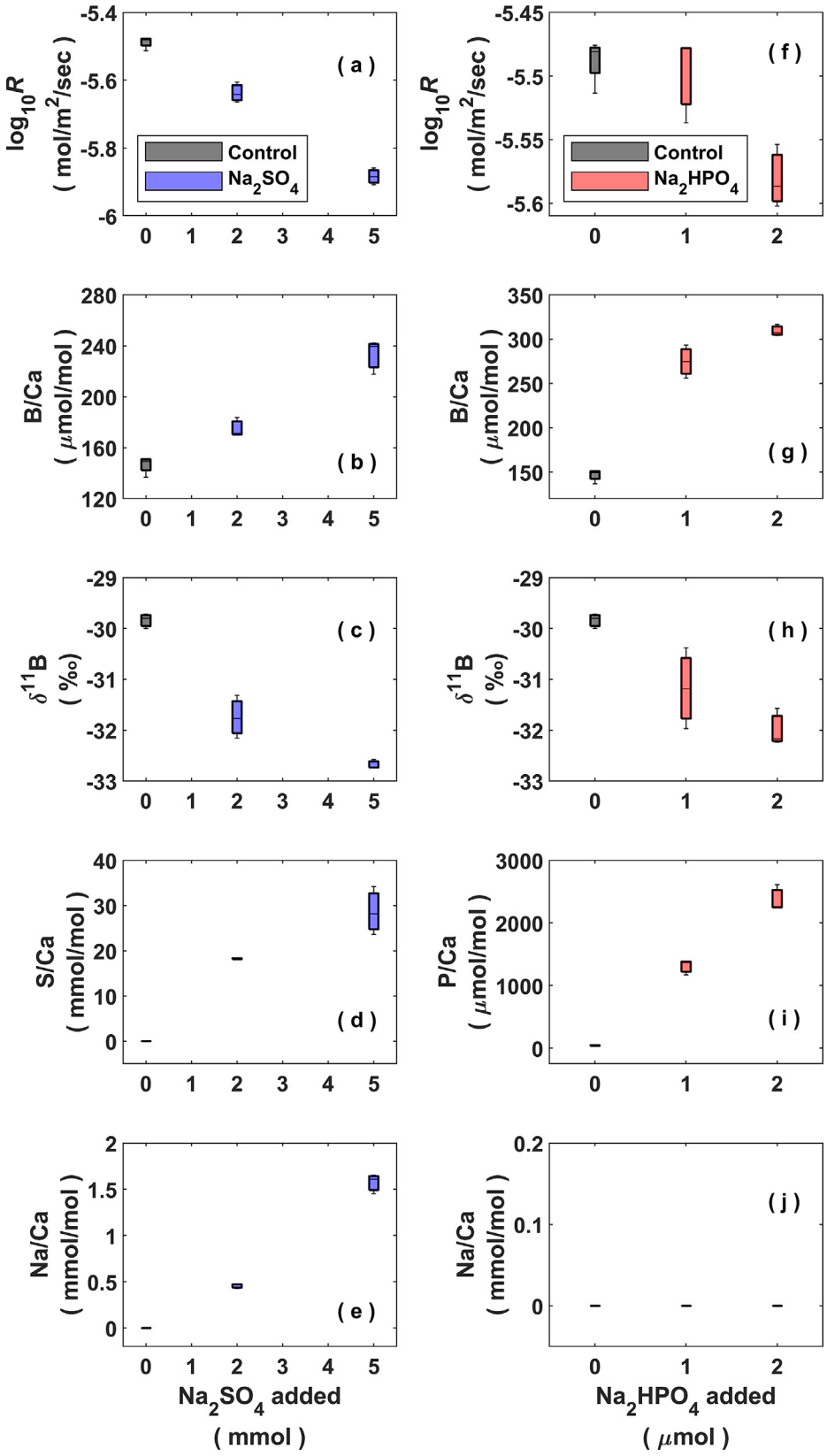

Fig. 5. Summary display of the changes in $\log_{10}R$, E/Ca and $\delta^{11}B$ caused by additions of Na_2SO_4 (left panels) and Na_2HPO_4 (right panels) to the control in the Phase 2 experiments.

the passage of B_4 across the DBL towards the calcite surface and subsequent incorporation. We also make a point that the experimental evaluations of the strength of a given ion as a PDI and the charge landscape in the calcite DBL referred here and in Henehan et al. (2022) were at equilibrium condition with no net calcite precipitation or dissolution (Cicerone et al., 1992; Zhang

Table 3
Summary of the experimental conditions and data from the second phase of the study (Phase-2 experiments). The data shown here are the average and 1σ St. Dev. of the results from replicate experiments at each condition.

	n	$\log_{10}R$ (mol/m^2/*sec*)	B/Ca (μmol/mol)	δ^{11}B (‰, NIST951)	S/Ca (mmol/mol)	P/Ca (μmol/mol)	Na/Ca (mmol/mol)
Control	4	−5.49 ± 0.02	146.6 ± 6.7	−29.84 ± 0.15	0	41.0 ± 5.1	0
+2 mmol Na_2SO_4	3	−5.64 ± 0.03	175.0 ± 7.6	−31.75 ± 0.42	18.3 ± 0.1	44.8 ± 1.5	0.46 ± 0.0
+5 mmol Na_2SO_4	3	−5.88 ± 0.02	233.1 ± 13.4	−32.68 ± 0.09	28.7 ± 5.3	58.2 ± 13.4	1.57 ± 0.1
+10 mmol NaCl	3	−5.46 ± 0.01	157.8 ± 5.2	−29.71 ± 0.21	0	51.5 ± 5.4	0.1 ± 0.1
+1 μmol Na_2HPO_4	3	−5.50 ± 0.03	274.7 ± 18.6	−31.18 ± 0.79	0	1307.4 ± 118.0	0
+2 μmol Na_2HPO_4	3	−5.58 ± 0.02	309.3 ± 6.5	−31.99 ± 0.37	0	2371.9 ± 207.8	0

and Austad, 2006; Alroudhan et al., 2016; Al Mohrouqi et al., 2017; Song et al., 2017). Hence, the applicability of the DBL effect proposed by Henehan et al. (2022) to inorganic $CaCO_3$ precipitation experiments that are obviously far from equilibrium is an open question.

The calcite seeds acted as a template and provided the reactive surface for heterogeneous calcite precipitation to follow. It is thus reasonable to assume that calcite growth mostly occurred as a result of orderly attachment of Ca-CO_3 building units to active growth kinks in our experiments (De Yoreo and Vekilov, 2003; De Yoreo et al., 2009), although one exception would be the Na_2-HPO_4 experiments in which ACC possibly played some roles for the experimental outcome (Section 4.2). Active kinks represent the sites of new calcite growth and initial point of contact upon incorporation of non-constituent *E* (Paquette and Reeder, 1995), including B. It follows that the abundance of growth kinks influence not only calcite precipitation kinetics but also the degrees of B incorporation. Dobberschütz et al. (2018) and Dove and Hochella (1993) suggested that the inhibitions on calcite precipitation and growth by SO_4^{2-} and HPO_4^{2-} (as reconfirmed in this study: see Section 5.2) are due to the adsorption of these oxyanions onto growth steps. This so-called kink blocking should impede the development of new and successive kinks and leave vacancies around advancing steps. While B_4 can be more readily accommodated in those vacancies due to unsatisfied Ca-O bond structures around the terminal Ca^{2+} or CO_3^{2-}, the net effect of reduced kink availability is anticipated to be negative for B incorporation.

In short, none of the scenarios for interactions of oxyanions (mostly SO_4^{2-}) with other ionic species in the solutions and with the calcite surface explored thus far seems to offer a convincing explanation for the apparently reversed kinetic effects on B/Ca and δ^{11}B (λ_B and $^{11}\varepsilon_{Calcite\text{-}B4}$) in the presence of SO_4^{2-} (Fig. 7).

5.4. Crystallographic considerations

Calcite can accommodate a range of non-constituent anions, and this is thought to occur mainly as a result of their initial interactions at growth kinks followed by eventual substitutions into CO_3 sites in the lattice (Kitano et al., 1975; 1978; Hemming et al., 1995; Balan et al., 2016; Kontrec et al., 2004; Busenberg and Plummer, 1985; Staudt et al., 1994; Okumura et al., 2018; Balan et al., 2014; Alexandratos et al., 2007; Tang et al., 2007). Because the amounts of those initial binding and terminal incorporation sites are not infinite, it is natural to presume that oxyanions introduced into our experimental solutions would compete with B (mostly as B_4: see Section 2) for those sites. Taking SO_4^{2-} as an example, free un-complexed SO_4^{2-} ions in our Na_2SO_4 addition experiments were roughly 9 to 57 times more abundant than free B_4 ions (Table-S1). With that, the chance of B_4 to interact with the growth kinks and incorporated into CO_3 sites could have been easily overwhelmed by SO_4^{2-}. We note, however, that not all calcite growth kinks are geometrically identical, such that the ones along the acute growth steps are spatially more constrained than those along the obtuse growth steps (Hemming et al., 1995; Staudt et al., 1994: see Fig. 8b). Staudt et al. (1994) conducted electron probe microanalysis on calcite crystals and found greater abundance of S derived from SO_4^{2-} along the obtuse growth steps. Hemming et al. (1998) used the same approach and found clear B enrichments along the acute steps (although this seems to somewhat contradict with Ruiz-Agudo et al. (2012), who observed more direct interactions between aqueous B species and the calcite surface along obtuse steps using an *in-situ* atomic force microscopy). If the opposing intra-crystal B and S zonation patterns (Staudt et al., 1994; Hemming et al., 1998) are correct, then there may be no direct competitions between B and SO_4^{2-} for binding/incorporation sites. It is unknown if P and N derived from the oxyanions tested here similarly possess unique zonation patterns in calcite due to the lack of direct observational evidence. P is thought to be incorporated into calcite as PO_4^{3-} (Ishikawa and Ichikuni, 1981; Mucci, 1986; Mason et al., 2007). Considering the commonality as tetrahedral oxyanions (Table-1), PO_4^{3-} may behave like SO_4^{2-} and SeO_4^{2-} (Staudt et al., 1994) and concentrate along obtuse steps. But it is equally possible that its site-specific preference may overlap with B, as other tetrahedral oxyanions such as AsO_4^{3-} and CrO_4^{2-} are found to be more concentrated along acute steps (Alexandratos et al., 2007; Tang et al., 2007). Regardless of whether they pose direct competitions with B for binding and/or incorporation sites, however, it is important to realize that both scenarios do not offer a convincing explanation for the enhancement of B incorporation upon SO_4^{2-} and HPO_4^{2-} additions into experimental solutions.

Experimental and computational studies suggest that SO_4^{2-} incorporation into calcite occurs due to substitutions with CO_3 without any coordination change (Busenberg and Plummer, 1985; Staudt et al., 1994; Kontrec et al., 2004; Okumura et al., 2018; Barkan et al., 2020; Balan et al., 2014). In this mode, three oxygen atoms comprising the basal plane of the SO_4^{2-} tetrahedron settle into the planar trigonal CO_3 space in the lattice. But the remaining apical oxygen is out of the CO_3 plane, which stretches the calcite unit cell along the *c*-axis direction and causes notable lattice distortion (Kontrec et al., 2004; Okumura et al., 2018; Goetchl et al., 2019: see Fig. 7). This is in line with Vavouraki et al. (2008), who found about 1 Å increase in the height of growth steps for calcite grown in the presence of SO_4^{2-}, compared to those formed in SO_4^{2-} free solution. Our SEM and XRD data clearly indicate that the integrity of the calcite crystal structure was compromised by SO_4^{2-} additions as well (Fig. 1 and Fig. 2). Based on inorganic calcite precipitation experiments, Goetschl et al. (2019) found that progressive SO_4^{2-} additions into growth solutions lead to a robust decline in the extent of Mg incorporation and elongation of the calcite unit cell along the *c*-axis due to incorporation of SO_4^{2-} into the calcite lattice. This necessitates Mg that replaces physically larger Ca to establish longer bonds with neighboring oxygen atoms of CO_3 to be present in the lattice, making the condition more unfavorable for incorporation. However, we presume that the same lattice distortions caused by SO_4^{2-} could work in favor for B incorporation (Fig. 8cd). Recall from Section 2 and

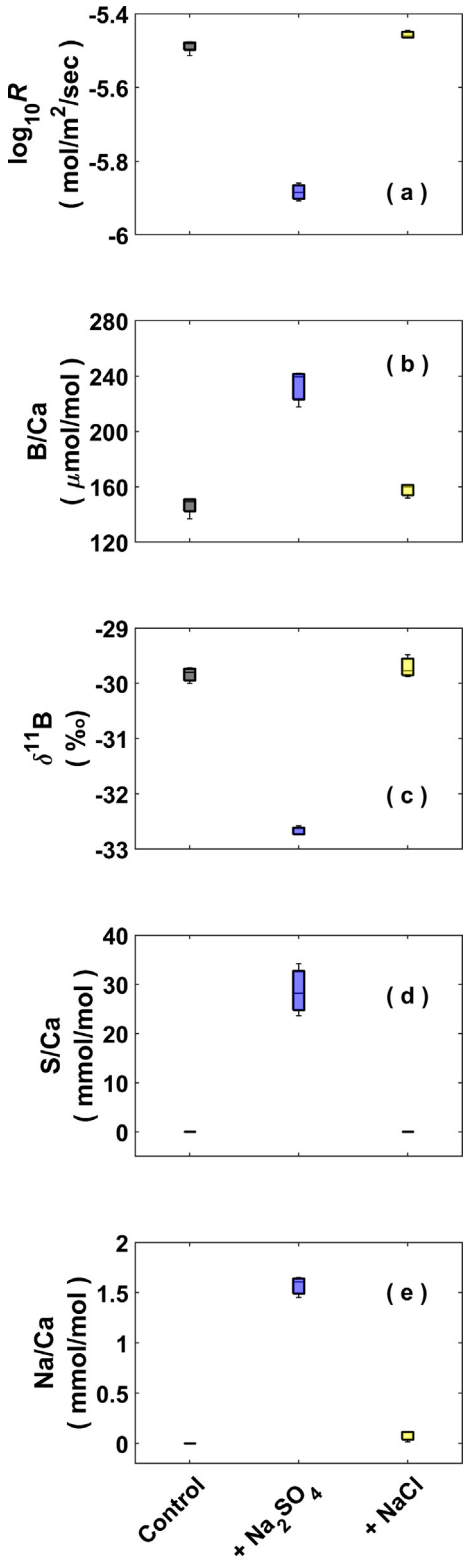

Fig. 6. The results from the Phase-2 cross experiments, in which the impact of addition of 5 mmol of Na_2SO_4 and 10 mmol of NaCl on calcite precipitation rate, *E*/Ca and $\delta^{11}B$ was compared. Only the Na_2SO_4 addition (but not the NaCl addition) caused notable changes in the experimental outcome.

Section 5.2 that, despite the evidence for some B_3 contributions, the canonical view of the B_4 dominance for B incorporation is still supported by isotopic evidence. Relative to B_3, B_4 is less compatible with the structural CO_3 sites and more prone to detachment from the calcite surface (Branson, 2018; Farmer et al., 2019). The key issue here is that B_4 (and its supposedly trigonal derivatives that ultimately end up in the lattice as structural species; Balan et al. (2016)) are physically larger than CO_3 (Table 1). But the lattice distortion, or specifically the lattice relaxation caused by SO_4^{2-} incorporation, could lessen this physical barrier and help retain tetrahedral B_4 that would otherwise be easily detached from the calcite surface. This proposed mechanism can simultaneously explain the increase in calcite S/Ca as well as λ_B and a decrease in $^{11}\varepsilon_{Calcite\text{-}B4}$ towards the value of 0 due to SO_4^{2-} additions. Note that SO_4^{2-} additions also decreased $\log_{10}R$ (Figs. 3–6). Within the framework of normal kinetic effects, this is expected to increase B_3 contributions for B incorporation into calcite as summarized in Section 5.2 and Fig. 7. However, our data demonstrate that the lattice distortion caused by SO_4^{2-} apparently imposed greater controls on B incorporation than normal kinetic effects in our experiments (Fig. 7).

Incorporation of PO_4^{3-} into the calcite is likely enabled by substitutions with CO_3 (Ishikawa and Ichikuni, 1981; Mucci, 1986; Mason et al., 2007), as verified for similarly tetrahedral SO_4^{2-} (see above) and SeO_4^{2-} (Reeder et al., 1994). Moreover, Ishikawa and Ichikuni (1981) suggested the replacement of three units of CO_3 in calcite by two units of PO_4^{3-} for the electro-neutrality to be maintained. As PO_4^{3-} is even larger than SO_4^{2-} (Table 1), the lattice deformation can be substantial (particularly if PO_4^{3-} incorporation follows the scheme by Ishikawa and Ichikuni, 1981). Our XRD data show the most significant broadening of the calcite d_{104} peak in a sample from the Na_2HPO_4 addition experiments (Fig. 2g), which points to poor sample crystallinity. Hence, the same mechanism appears to be responsible for the reverse kinetic effects on calcite B/Ca and $\delta^{11}B$ observed in our experiments with SO_4^{2-} and HPO_4^{2-} additions (Fig. 5).

We are not aware of experimental studies that confirmed or quantified the presence of NO_3^- in inorganic calcite (to the best of our knowledge). Molecular dynamic simulations by Hoffman et al. (2016) suggest strong interactions between NO_3^- and the calcite surface, such that NO_3^- can be 25 % more concentrated than CO_3^{2-} ions in the direct vicinity of the surface. They argued that such a strong affinity towards calcite surface may lead to eventual CO_3 substitutions by NO_3^-. Kontrec et al. (2004) employed a combination of analytical tools and examined the crystallinity of calcite formed via mixing of $Ca(OH)_2$ solution and $NaNO_3$ dissolved in CO_2-bubbled H_2O and argued that NO_3^- incorporation in calcite does not cause notable lattice disorder. However, this conclusion assumes that incorporation did indeed occur, albeit without definitive evidence. But this seems plausible, given the versatility of calcite in accommodating a wide range of ions differing in coordination, size, charge, and valence state. And if NO_3^- incorporation does occur, it is conceivable that it proceeds via substitutions with CO_3 because they share the same planar trigonal coordination. Moreover, lattice disorder associated with this substitution should be small (unlike the case with SO_4^{2-} and PO_4^{3-}) due to the relatively small size discrepancy between CO_3^{2-} and NO_3^- (Table 1). This is consistent with our SEM and XRD data (Fig. 1 and Fig. 2). This could explain why the B/Ca data from NO_3^- addition experiments were essentially no different from the control (Fig. 3). Studies that have investigated interactions between NO_2^- and calcite are lacking, which makes our interpretations speculative. If the degrees of B incorporation in calcite are tied to the lattice deformation (or lack thereof) invoked by oxyanions, then the lack of notable B/Ca differences between the control and $NaNO_2$ addition experiments would imply limited lattice distortion from NO_2^- incorporation (if it does occur).

As described in Section 2, $\delta^{11}B$ and other constraints from prior studies support the notion that small fractions of B in calcite must be derived from aqueous B_3. Balan et al. (2016) suggested that B_3

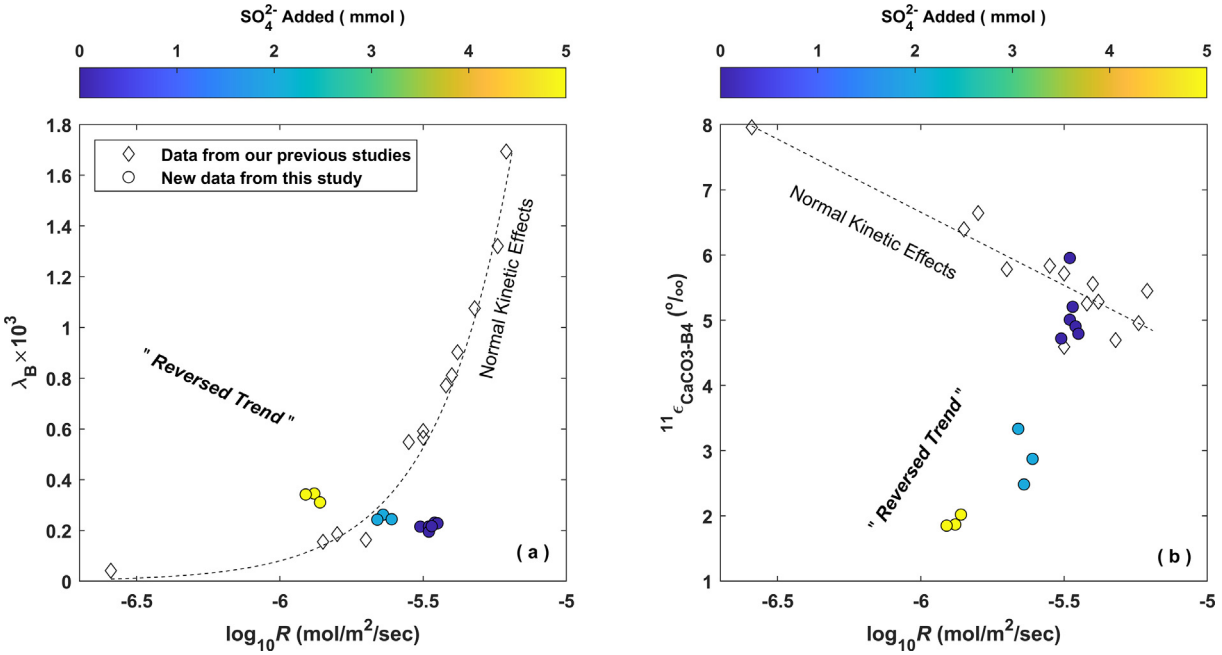

Fig. 7. Comparison of the new B/Ca and $\delta^{11}B$ data from our Phase-2 experiments (control, Na_2SO_4 and NaCl experiments are compiled) to those from our previous experimental studies (B/Ca and $\delta^{11}B$ data are from Uchikawa et al. (2015) and Farmer et al. (2019), respectively). The data are expressed as λ_B and $^{11}\varepsilon_{CaCO3\text{-}B4}$ (apparent B partition coefficient and ^{11}B enrichment in $CaCO_3$ relative to aqueous B_4, respectively: see Eq. (6) and Eq. (7)) and plotted as a function of $\log_{10}R$, where R is calcite precipitation rates in mol/m^2/*sec*. The color gradient applied to the new data from the present study (circles) reflect the amount of SO_4^{2-} added to the experimental solutions. As indicated by the data from our previous studies (open diamonds), when changes in R depend only on the degree of $CaCO_3$ saturation, the normal kinetic effects impose λ_B and $^{11}\varepsilon_{CaCO3\text{-}B4}$ to exponentially increase and almost linearly decrease as a function of $\log_{10}R$. In the present study, changes in R were driven by the addition of SO_4^{2-} (calcite nucleation/precipitation inhibitor) with no changes in the degree of saturation. Under this circumstance, changes in λ_B and $^{11}\varepsilon_{CaCO3\text{-}B4}$ as a function of $\log_{10}R$ are reverse of what can be expected from the normal kinetic effects. Lastly, note that there should be no methodological biases (*e.g.*, Farmer et al., 2016) in comparing the $\delta^{11}B$ data from Farmer et al. (2019) and our study, as both were based on multi-collector ICPMS using similar analytical methods.

can be directly entrapped from solution as non-structural components in porous and hydrous $CaCO_3$ phase of low crystallinity (*e.g.*, ACC). Thus, in Uchikawa et al. (2017), we postulated that the increase in calcite B/Ca caused by Na_2HPO_4 additions to Mg-free ASW can be explained by entrapment of B_3 in ACC that could form in P-bearing solutions (Dove and Hochella, 1993). The amorphous phase in the samples from the Na_2HPO_4 addition experiments (Fig. 2c) can be composed of ACC (Blue et al., 2017). Evans et al. (2020) analyzed various *E*/Ca ratios in ACC precipitated from seawater and found that the degrees of B incorporation are orders of magnitude higher in ACC than those for inorganic calcite. This is in line with Mavromatis et al. (2021), who traced the changes in B contents and $\delta^{11}B$ over the course of transformation of ACC into calcite. Moreover, their data (B-2 and B-3 experiments presented in Table 2 of their paper) show that $\delta^{11}B$ of ACC immediately after its formation is offset from $\delta^{11}B$ of B_4 by only ~1 ‰. This implies that B entrapped in ACC is mostly from B_4, which is in accordance with a robust positive covariance between B/Ca of ACC and solution pH noted by Evans et al. (2020). The new evidence from Evans et al. (2020) and Mavromatis et al. (2021) signifies that our conjecture of substantial B_3 enrichment in ACC presented in Uchikawa et al. (2017) is inaccurate. Moreover, a combination of severe lattice distortion caused by PO_4^{3-} incorporation into calcite and additional B_4 contributions from co-precipitating ACC can explain why the Na_2HPO_4 additions of only a few μmol led to remarkably strong responses in sample B/Ca and $\delta^{11}B$ (Fig. 3 and Fig. 5).

5.5. Parallel consideration of Na incorporation and the issue of charge compensation

In this work, only the samples from the Phase-2 experiments were analyzed for Na/Ca. Albeit limited in numbers, it is worthwhile to discuss available Na/Ca data in light of the growing interest in the use of Na/Ca in marine carbonates as a tracer for past changes in seawater salinity or $[Ca^{2+}]$ (*e.g.*, Wit et al., 2013; Bertlich et al., 2018; Hauzer et al., 2018; Zhou et al., 2021) and the possible role of Na^+ in providing charge compensation when B_4 substitutes CO_3 in $CaCO_3$ (Henehan et al., 2022; Balan et al., 2016).

In previous studies (Ishikawa and Ichikuni, 1984; Busenberg and Plummer, 1985; Füger et al., 2019; Devriendt et al., 2021), Na incorporation into inorganic calcite was shown to depend on several factors, including solution Na/Ca concentration or activity ratios, calcite precipitation rates *R*, carbonate chemistry parameters (pH and DIC speciation), and calcite S/Ca ratios. In our Phase-2 experiments, raising solution $[Na^+]$ from the control condition by way of adding NaCl resulted in virtually no change in *R* and Na/Ca (Fig. 6). But increasing solution $[Na^+]$ by Na_2SO_4 additions elevated calcite Na/Ca, despite the decrease in *R*. The negative correlation between Na/Ca and *R* observed in our Na_2SO_4 experiments is exactly the opposite of what can be expected from the known kinetic effects for Na incorporation (Füger et al., 2019; Devriendt et al., 2021). Meanwhile, the positive covariance between calcite Na/Ca and S/Ca found in our experiments is consistent with Busenberg and Plummer (1985). Busenberg and Plummer (1985) argued that the Na incorporation into calcite depends on the abundance of crystallographic defects, which can increase as CO_3 in the lattice is replaced by SO_4. However, Yoshimura et al. (2017) argued that Na does occur as structural species via substitutions of two units of Ca^{2+} by two Na^+ and leaving one CO_3 vacancy in the lattice to achieve neutrality based on synchrotron X-ray analyses on some marine biogenic calcite. Direct substitutions of Ca^{2+} by Na^+ should be more efficient when atomic spacing in the lattice is somehow loosened (as we made the case for B incorporation in Section 5.4),

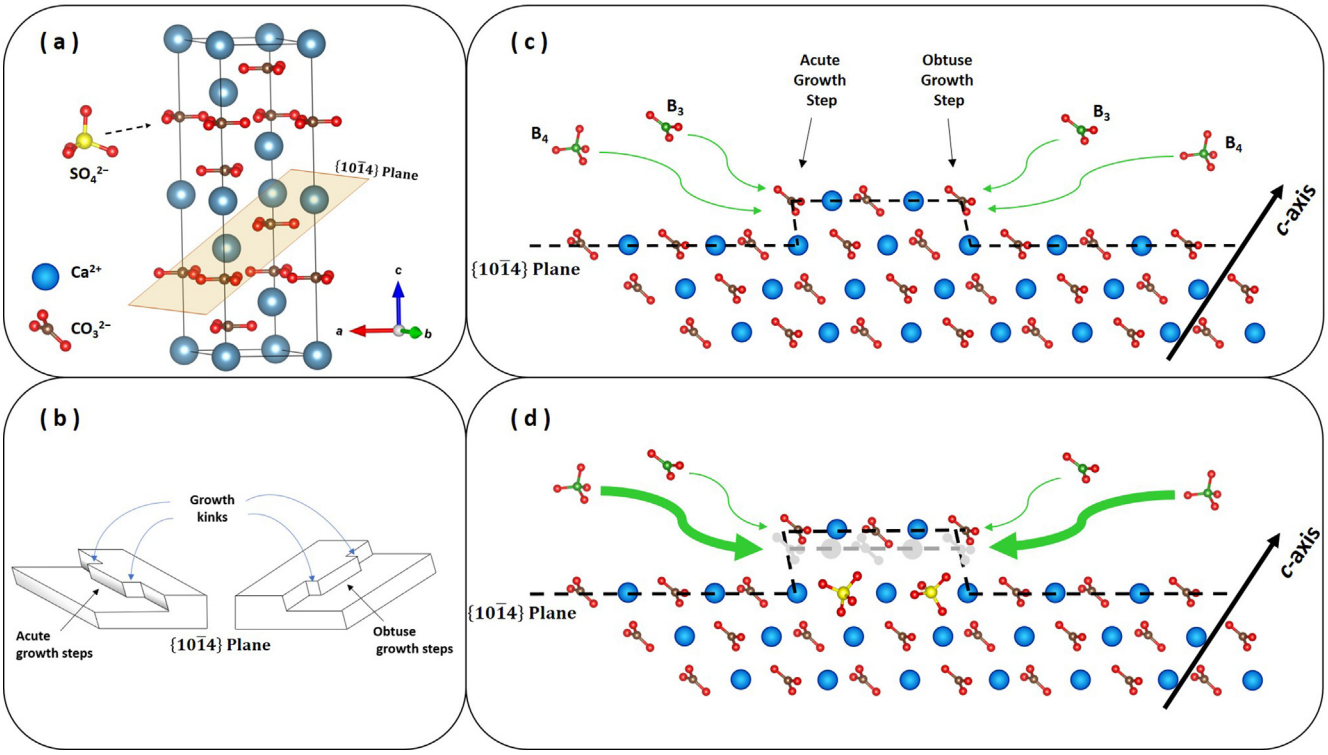

Fig. 8. (a) Illustration of the calcite unit cell using the VESTA 3D vitalization software (https://jp-minerals.org/vesta/en), with an overlay of the $\{10\bar{1}4\}$ cleavage/growth planes relative to the *c*-axis that is perpendicular to the CO_3 planes. As detailed in Section 5-4, tetrahedral oxyanions such as SO_4^{2-} can substitute CO_3 in the lattice. (b) Growth features (steps and kinks) that develop on an exposed $\{10\bar{1}4\}$ plane due to formation of spiral growth hillocks (see Larsen et al., 2010). Kinks that develop along the obtuse steps are geometrically larger and more open than those along the acute steps (see Hemming et al., 1998). (c) Undisturbed atomic arrangement and development of growth steps on an exposed $\{10\bar{1}4\}$ plane, following Larsen et al. (2010). See Section 5.2 and Farmer et al. (2019) for mechanistic model for interaction and incorporation of B_3 and B_4 at kinks during calcite growth. (d) A hypothetical case for substitution of CO_3 in the lattice by SO_4^{2-}. While three basal oxygens can fit into the CO_3 plane, the apical oxygen of SO_4^{2-} is out of the CO_3 plane. This is known to dilate the calcite unit cell along the *c*-axis direction (also see panel a) and increase the height of growth steps in comparison to the undisturbed case (shadowed in panel d: Vavouraki et al., 2008). In turn, this supposedly improves the retainment of tetrahedral B_4 at growth kinks and enhances the overall B incorporation into calcite. The same scenario likely holds for CO_3 substitutions by PO_4^{3-}, however, the effect is expected to be more substantial due to the size difference between SO_4^{2-} and PO_4^{3-} (see Table 1). Note that the size of the atoms and ionic species shown here is not necessarily at the exact scale relative to each other. We also emphasize that this is a very simplified 2-dimensional conceptual illustration. Realistic 3-dimensional atomic and bonding rearrangements caused by CO_3 substitutions by tetrahedral oxyanions in the lattice are more complex (*e.g.*, Reeder et al., 1994; Alexandratos et al., 2007).

given that the ionic radius of Na^+ is slightly larger than Ca^{2+} (1.02 Å vs 1.00 Å: Shannon, 1976) when both are in octahedral configuration (as expected for the need of bond formations with the six nearest oxygens of CO_3 in the calcite lattice). Therefore, irrespective of whether Na occurs as non-structural (Busenberg and Plummer, 1985) or structural components (Yoshimura et al., 2017), the degrees of crystallinity are expected to be an important factor for Na incorporation into calcite. Kontrec et al. (2004) experimentally found that Cl^- incorporation into calcite causes no major distortions in the lattice, unlike the case for SO_4^{2-} incorporation. This could explain why the Na_2SO_4 additions – but not the NaCl additions – boosted calcite Na/Ca in our experiments against the known kinetic effects (Füger et al., 2019; Devriendt et al., 2021). Our data are insufficient to decipher whether Na in calcite occurs as structural or non-structural components. But they provide some unique perspectives on the development of Na/Ca of biogenic calcite as a paleo-proxy for past changes in seawater chemistry (*e.g.*, Wit et al., 2013; Bertlich et al., 2018; Hauzer et al., 2018; Zhou et al., 2021). For example, the lack of change in calcite Na/Ca in response to increasing solution $[Na^+]$ by NaCl addition revealed here is counterintuitive to the foundation of the proxy as currently conveyed (Zhou et al., 2021), that is the dependence of calcite Na/Ca to seawater Na/Ca concentration or activity ratios. The strong positive covariance between calcite Na/Ca and S/Ca (also see Busenberg and Plummer, 1985) further urges a careful consideration of SO_4^{2-} for the establishment or use of Na/Ca in biogenic calcite as a paleo-salinity proxy (Wit et al., 2013; Bertlich et al., 2018).

Data from culture experiments by Allen et al. (2011; 2012) and a core-top study by Henehan et al. (2015) show that B/Ca in several planktic foraminifers increase with salinity. Balan et al. (2016) argued that coupled Na^+–Ca^{2+} and B_4 – CO_3^{2-} substitutions represent a probable mechanism for effectively resolving the charge imbalance associated with B_4 incorporation into calcite. Thus, they interpreted the salinity effects on foraminiferal B/Ca to be the result of an inevitable increase in seawater $[Na^+]$ with salinity. The importance of this coupled substitution as a charge compensation mechanism is further supported by a strong positive correlation between B/Ca and Na/Ca in inorganic calcite and aragonite observed in a recent experimental study by Henehan et al. (2022). This correlation is also apparent in this study, when the data from the Phase-2 control, Na_2SO_4 and NaCl addition experiments are compiled (Fig. 9). Furthermore, the regression slopes for the correlation between B/Ca and Na/Ca revealed here and in Henehan et al. (2022) are stunningly similar. This could indicate a mechanistic link related to charge compensation between B_4 and Na incorporation. Yet, as opposed to the interpretation by Balan et al. (2016), we argue that the abundance or availability of ionic agents capable of providing charge compensation (Na^+ in this case) neither enhance nor suppress the degrees of B incorporation. Otherwise, additions of 10 mmol of NaCl in our cross experiments should have elevated B incorporation (but see Figs. 4 and 5).

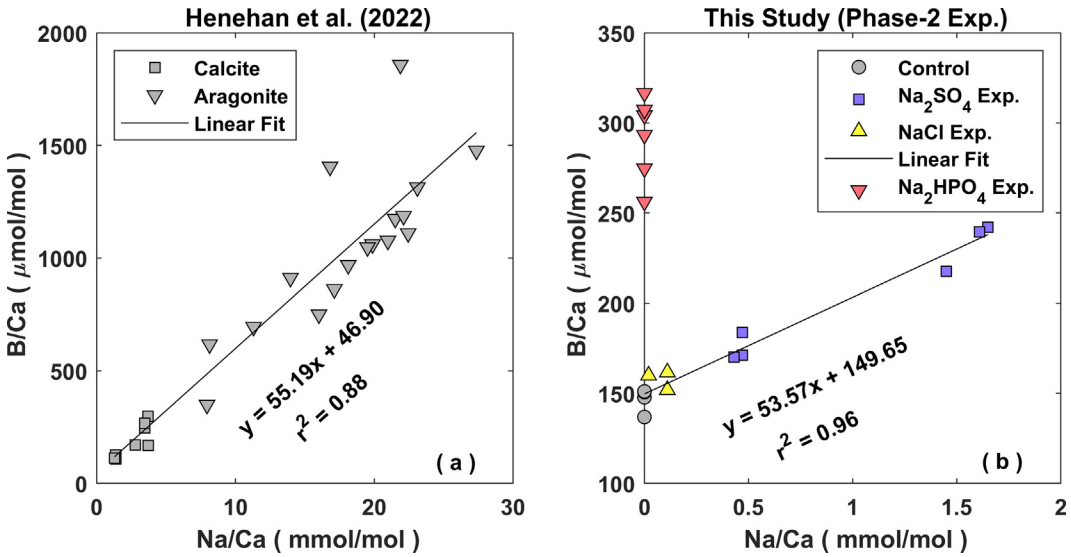

Fig. 9. Relationship between B/Ca and Na/Ca of laboratory-grown inorganic $CaCO_3$ observed in Henehan et al. (2022) (a) and in calcite samples produced from our Phase-2 experiments (b). The equation for the covariance derived from linear regression in Henehan et al. (2022) is composite for both calcite and aragonite samples. The same for ours takes account the data from the control, Na_2SO_4 and NaCl addition experiments only and excludes the data from the Na_2HPO_4 experiments (see Section 5.5 for details). Notice the stunningly similar slopes for the covariance in both studies, despite the difference in experimental conditions (*e.g.*, solution matrix, calcite-aragonite composite vs strictly calcite, seeded vs non-seeded precipitation approach, and so on).

Our new data also imply that the salinity effect on B/Ca confirmed in both foraminiferal (Allen et al., 2011; 2012; Henehan et al., 2015) and inorganic calcite (Uchikawa et al., 2017) may be rooted in consequential changes in seawater [SO_4^{2-}], rather than [Na^+].

Note that the relationship between calcite B/Ca and Na/Ca completely breaks down for the Na_2HPO_4 addition experiments (see Fig. 9b), because calcite Na/Ca in those experiments are invariant (Table 3 and Fig. 6e). This is puzzling because, as is the case with SO_4^{2-}, it appears conceivable that the lattice distortion caused by PO_4^{3-} could enhance Na incorporation. Though this is speculative, the disparity in Na/Ca data between the Na_2SO_4 and Na_2HPO_4 experiments (Fig. 5e vs 5j) could possibly lie in the issue of charge compensation. When CO_3 in calcite is replaced by SO_4^{2-}, there is no charge imbalance to be resolved. Yet, substitution between B_4 and CO_3^{2-} during calcite precipitation (the extent of which is apparently sensitive to lattice distortion caused by SO_4^{2-}, see Section 5.4) leaves one unit of e^- deficit in calcite, which can be neutralized by concurrent replacement of Ca^{2+} by Na^+ (Balan et al., 2016; Henehan et al., 2022; Fig. 9). On the contrary, substitution by PO_4^{3-} itself leads to a charge imbalance of one unit of e^- excess (unless multiple units of CO_3^{2-} and PO_4^{3-} are simultaneously substituted: *e.g.*, Ishikawa and Ichikuni, 1981). One possible mode for neutralization that can align with our experimental results would be a coupled substitution, where 2 units of CO_3^{2-} are substituted by 1 unit each of PO_4^{3-} and B_4 in the lattice (Henehan et al., 2015). But note that the aqueous phosphate speciation at our experimental pH was dominated by HPO_4^{2-} (Section 4.1). If HPO_4^{2-} represent the starting point of incorporation (*i.e.*, initial adsorption to the calcite surface) that ultimately ends up in the lattice as PO_4^{3-} (Mason et al., 2007), then the process must involve deprotonation. The deprotonated H^+ may interact and bind with one of the four OH^- arms of B_4 at the calcite surface. This can promote coordination change for tetrahedral B_4 to the planar trigonal form via dehydration (*e.g.*, Balan et al., 2016) and theoretically resolve the charge imbalance associated with substitutions of CO_3^{2-} by B_4. In either case, there is no charge imbalance that needs to be compensated for by Na^+. Though more thorough investigations are needed, these scenarios appear feasible for our fairly simplified experimental solutions.

6. Conclusions and Implications

In this study, we found that the presence of NO_3^- and NO_2^- in experimental solutions have no impact on precipitation kinetics of and B/Ca in inorganic calcite. In a stark contrast, SO_4^{2-} and HPO_4^{2-} additions led to a substantial increase in calcite B/Ca but a concurrent decline in $\delta^{11}B$ towards the values expected for aqueous B_4. This isotopic constraint signifies that the increase in calcite B/Ca reflects enhancement for incorporation of B_4. Along with the changes in calcite B/Ca and $\delta^{11}B$, SO_4^{2-} and HPO_4^{2-} additions caused a substantial decrease in calcite precipitation rate *R*. The observed enhancement of B_4 incorporation with the decrease in *R* is the opposite of what can be expected from the framework of the normal kinetic effects for B incorporation (Branson, 2018; Farmer et al., 2019). These paradoxical results can be explained by the lattice distortions arising from substitutions of planar trigonal CO_3 in the calcite lattice by physically larger SO_4^{2-} and PO_4^{3-}. More specifically, expansion of the calcite unit cells caused by these tetrahedral oxyanions lessens the physical barrier for similarly tetrahedral (yet comparatively smaller) B_4 to be placed into the CO_3 sites. This increases the probability of B_4 to be successfully incorporated into calcite as the structural species after initial adsorption to growth kinks. We note that ACC may be an additional contributing factor for the extremely strong B/Ca responses to the Na_2HPO_4 additions on the order of just a few μmol. Our B/Ca and Na/Ca data show a certain level of consistency with Henehan et al. (2022), suggesting that Na^+ likely plays an important role for charge compensation upon exchange of CO_3^{2-} by B_4 (Balan et al., 2016; Henehan et al., 2022). At the same time, however, our data seem to show the possibility of other modes of charge compensation that do not involve Na^+.

We reemphasize that the changes in calcite B/Ca and $\delta^{11}B$ resulted from the Na_2SO_4 additions in our experiments are strictly due to changing solution [SO_4^{2-}], with no other forced changes in solution chemistry (*e.g.*, pH). Also, there is an indication that SO_4^{2-} incorporation itself is sensitive to the state of dissolved carbonate chemistry and calcite precipitation kinetics (Wynn et al., 2018). This means that the observed impacts of SO_4^{2-} on B/Ca and $\delta^{11}B$ can be more accentuated if our control/baseline solution

chemistry is set at different conditions. In our Phase-2 experiments, 5 mmol of SO_4^{2-} addition led to changes in calcite B/Ca by over 80 μmol/mol and in $\delta^{11}B$ by ~2.8 ‰ (Fig. 5). If a similar SO_4^{2-} impact can be verified in biogenic carbonates, this would be alarming for the use of the B/Ca and $\delta^{11}B$ as paleo-proxies for long-term changes in ocean carbonate chemistry, given the homogeneity and high concentration of SO_4^{2-} in seawater (unlike other non-conservative and bio-reactive oxyanions tested here) and substantial changes in seawater [SO_4^{2-}] over geologic timescales (Horita et al., 2002; Lowenstein et al., 2003; Brennan et al., 2013; Algeo et al., 2015; Zeebe and Tyrrell, 2019). Similarly, our experimental results imply that variations in seawater phosphate concentration by only a few μmol (which is realistic) potentially pose major biases in B/Ca and $\delta^{11}B$. While a robust positive correlation between seawater phosphate and B/Ca of a planktic foraminiferal species is reported in a core-top study by Henehan et al. (2015), other core-top and sediment trap studies offer no evidence for such (Quintana Krupinski et al., 2017; Salmon et al., 2016). However, it is difficult to draw a firm conclusion from these field studies, as the data are simultaneously impacted by differences in other physicochemical properties of seawater.

The reactive surface of calcite crystals was in direct contact with experimental solutions dosed with various oxyanions in our experiments. Contrastingly, calcification in marine calcifiers occurs in specialized microenvironments that are isolated and chemically altered from the ambient seawater (de Nooijer et al., 2014). In that sense, the dependence of calcite B/Ca and $\delta^{11}B$ to changes in sulfate and phosphate concentration revealed here may not be directly applicable to the B paleo-proxies in marine biogenic calcite. Nevertheless, taking foraminiferal calcite as an example, there are common B/Ca responses between inorganic and biogenic calcite (at least trend-wise) to changes in some physicochemical parameters (Uchikawa et al., 2015; 2017; Allen et al., 2011; 2012; Henehan et al., 2015; Haynes et al., 2017; 2019). In that light, our novel experimental results signify the need for further and direct evaluations of the dependence of B proxies to changes in seawater sulfate and phosphate concentrations.

Declaration of Competing Interest

The authors declare that they have no known competing financial interests or personal relationships that could have appeared to influence the work reported in this paper.

Acknowledgements

We are grateful to Colin Carney (UCSC Stable Isotope Lab), Kazuhide Nagashima (UH WMK Cosmochemistry Lab) and Przemyslaw Dera (UH X-ray Atlas Diffraction Lab) for their support on $\delta^{13}C$, SEM, and XRD work. We thank Caroline Thaler and an anonymous reviewer for their helpful and constructive comments. This work was supported by US NSF grants #2024631 (JU, NP and DEP) and #1536743 (JU and REZ). SOEST pub. # 11621.

Appendix A. Supplementary material

Supplementary materials for this paper contains: Additional figures and Data table in which all experimental results and constraints for experimental solution chemistry are compiled.

Supplementary material to this article can be found online at https://doi.org/10.1016/j.gca.2022.12.018.

References

Al Mohrouqi, D., Vinogradov, J., Jackson, M.D., 2017. Zeta potential of artificial and natural calcite in aqueous solution. Adv. Colloid Interface Sci. 240, 60–76.

Alexandratos, V.G., Elzinga, E.J., Reeder, R.J., 2007. Arsenate uptake by calcite: Macroscopic and spectroscopic characterization of adsorption and incorporation mechanisms. Geochim. Cosmochim. Acta 71, 4172–4187.

Algeo, T.J., Luo, G.M., Song, H.Y., Lyons, T.W., Canfield, D.E., 2015. Reconstruction of secular variation in seawater sulfate concentrations. Biogeosciences 12, 2131–2151.

Allen, K.A., Hönisch, B., Eggins, S.M., Yu, J., Spero, H.J., Elderfield, H., 2011. Controls on boron incorporation in cultured tests of the planktic foraminifer *Orbulina universa*. Earth Planet. Sci. Lett. 345–348, 203–211.

Allen, K.A., Hönisch, B., Eggins, S.M., Rosenthal, Y., 2012. Environmental controls on B/Ca in calcite tests of the tropical planktic foraminifer species *Globigerinoides ruber* and *Globigerinoides sacculifer*. Earth Planet. Sci. Lett. 351–352, 270–280.

Alroudhan, A., Vinogradov, J., Jackson, M., 2016. Zeta potential of intact natural limestone: impact of potential-determining ions Ca, Mg and SO_4. Colloids Surf. A: Physicochem. Eng. Asp. 493, 83–98.

Balan, E., Blanchard, M., Pinilla, C., Lazzeri, M., 2014. First-principles modeling of sulfate incorporation and 34S/32S isotopic fractionation in different calcium carbonates. Chem. Geol. 374–375, 84–91.

Balan, E., Pietrucci, F., Cervais, C., Blanchard, M., Schott, J., Gaillardet, J., 2016. First-principles study of boron speciation in calcite and aragonite. Geochim. Cosmochim. Acta 193, 119–131.

Balan, E., Noireaux, J., Mavromatis, V., Saldi, G.D., Montouillout, V., Blanchard, M., Pietrucci, F., Gervais, C., Rustad, J.R., Schott, J., Gaillardet, J., 2018. Theoretical isotopic fractionation between structural boron in carbonates and aqueous boric acid and borate ion. Geochim. Cosmochim. Acta 222, 117–129.

Ball, J., Nordstrom, D., 1991. User's manual for WATEQ4F with revised thermodynamic database and test cases for calculating speciation of major, trace and redox elements in natural waters. U.S. Geological Survey Water-Resources Investigation Report, 91–183.

Barkan, Y., Paris, G., Webb, S.M., Adkins, J.F., Halevy, I., 2020. Sulfur isotope fractionation between aqueous and carbonate-associated sulfate in abiotic calcite and aragonite. Geochim. Cosmochim. Acta 280, 317–339.

Bertlich, J., Nürnberg, D., Hathorne, E.C., de Nooijer, L.J., Mezger, E.M., Kienast, M., Nordhausen, S., Reichard, G.-J., Schönfeld, J., Bijma, J., 2018. Salinity control on Na incorporation into calcite tests of the planktonic foraminifera Trilobatus sacculifer – Evidence from culture experiments and surface sediments. Biogeosciences 15, 5991–6018.

Blue, C.R., Giuffre, A., Mergelsberg, S., Han, N., De Yoreo, J.J., Dove, P.M., 2017. Chemical and physical controls on the transformation of amorphous calcium carbonate into crystalline $CaCO_3$ polymorphs. Geochim. Cosmochim. Acta 196, 179–196.

Branson, O., 2018. Chapter 4: Boron incorporation into marine $CaCO_3$. In: Marschall, H., Foster, G.L. (Eds.), Boron Isotopes. Advances in Isotope Geochemistry. Springer, pp. 71–105.

Brennan, S.T., Lowenstein, T.K., Cendon, D.I., 2013. The major-ion composition of Cenozoic seawater: the past 36 million years from fluid inclusions in marine halite. Am. J. Sci. 313, 713–775.

Brečević, L., Nielsen, A.E., 1989. Solubility of amorphous calcium carbonate. J. Cryst. Growth 98, 504–510.

Brown, P.W., Fulmer, M., 1991. Kinetics of hydroxyapatite formation at low temperatures. J. Am. Ceram. Soc. 74, 934–940.

Burton, E.A., Walter, L.M., 1990. The role of pH in phosphate inhibition of calcite and aragonite precipitation rates in seawater. Geochim. Cosmochim. Acta 54, 797–808.

Busenberg, E., Plummer, L.N., 1985. Kinetic and thermodynamic factors controlling the distribution of SO_4^{2-} and Na^+ in calcites and selected aragonites. Geochim. Cosmochim. Acta 49, 713–725.

Calvert, S.E., Pedersen, T.F., 2007. Elemental proxies for paleoclimatic and paleoceanographic variability in marine sediments: interpretation and application. In: Hillaire-Marcel, C., De Vernal, A. (Eds.), Developments in Marne Geology. Elsevier, pp. 567–644.

Cicerone, D.S., Regazzoni, A.E., Blesa, M.A., 1992. Electrokinetic properties of the calcite/water interface in the presence of magnesium and organic matter. J. Colloid Interface Sci. 154, 423–433.

Combes, C., Rey, C., 2010. Amorphous calcium phosphates: Synthesis, properties and uses in biomaterials. Acta Biomater. 6, 3362–3378.

de Nooijer, L.J., Spero, H.J., Erez, J., Bijma, J., Reichart, G.J., 2014. Biomineralization in perforate foraminifera. Earth Sci. Rev. 135, 48–58.

De Yoreo, J.J., Vekilov, P.G., 2003. Principles of crystal nucleation and growth. Rev. Mineral. Geochem. 54, 57–93.

De Yoreo, J.J., Zepeda-Ruiz, L.A., Friddle, R.W., Qiu, S.R., Wasylenki, L.E., Chernov, A. A., Gilmer, G.H., Dove, P.M., 2009. Rethinking classical crystal growth models through molecular scale insights: consequences of kink-limited kinetics. Cryst. Growth Des. 9, 5135–5144.

Devriendt, L.S., Mezger, E.M., Olsen, E.K., Watkins, J.M., Kaczmarek, K., Nehrke, G., de Nooijer, L.J., Reichart, G.-J., 2021. Sodium incorporation into inorganic $CaCO_3$ and implications for biogenic carbonates. Geochim. Cosmochim. Acta 314, 294–312.

Dobberschütz, S., Nielsen, M.R., Sand, K.K., Civioc, R., Bovert, N., Stipp, S.L.S., Andersson, M.P., 2018. The mechanisms of crystal growth inhibition by organic and inorganic inhibitors. Nat. Commun. 9, 1578.

Dorozhkin, S.V., 2010. Amorphous calcium (ortho)phosphates. Acta Biomater. 6, 4437.

Dove, P.M., Hochella, M.F., 1993. Calcite precipitation mechanisms and inhibition by orthophosphate: In situ observation by Scanning Force Microscopy. Geochim. Cosmochim. Acta 57, 705–714.

Evans, D., Gray, W.R., Rae, J.W.B., Greenop, R., Webb, P.B., Penkman, K., Kröger, R., Allison, N., 2020. Trace and major element incorporation into amorphous calcium carbonate (ACC) precipitated from seawater. Geochim. Cosmochim. Acta 290, 293–311.

Farmer, J.R., Hönisch, B., Uchikawa, J., 2016. Single laboratory comparison of MG-ICP-MS and N-TIMS boron isotope analyses in marine carbonates. Chem. Geol. 447, 173–182.

Farmer, J.R., Branson, O., Uchikawa, J., Penman, D.E., Hönisch, B., Zeebe, R.E., 2019. Boric acid and borate incorporation in inorganic calcite inferred from B/Ca, boron isotopes and surface kinetic modeling. Geochim. Cosmochim. Acta 244, 229–247.

Foster, G.L., Rae, J.W.B., 2016. Reconstructing ocean pH with boron isotopes in foraminifera. Annu. Rev. Earth Planet. Sci. 44, 207–237.

Foster, G.L., Pogge von Strandmann, P.A.E., Rae, J.W.B., 2010. Boron and magnesium isotopic composition of seawater. Geochem. Geophys. Geosyst. 11, Q08015.

Foster, G.L., 2008. Seawater pH, pCO_2 and $[CO_3^{2-}]$ variations in the Caribbean Sea over the last 130 kyr: a boron isotope and B/Ca study of planktic foraminifera. Earth Planet. Sci. Lett. 271, 254–266.

Füger, A., Konrad, F., Leis, A., Dietzel, M., Mavromatis, V., 2019. Effect of growth rate and pH on lithium incorporation in calcite. Geochim. Cosmochim. Acta 248, 14–24.

Gabitov, R.I., Rollion-Bard, C., Tripati, A., Sadekov, A., 2014. *In situ* study of boron partitioning between calcite and fluid at different crystal growth rates. Geochim. Cosmochim. Acta 137, 81–92.

Goetschl, K.E., Purgstaller, B., Dietzel, M., Mavromatis, V., 2019. Effect of sulfate on magnesium incorporation in low-magnesium calcite. Geochim. Cosmochim. Acta 265, 505–519.

Harper, D.T., Hönisch, B., Zeebe, R.E., Shaffer, G., Haynes, L.L., Thomas, E., Zachos, J.C., 2020. The magnitude of surface ocean acidification and carbon release during Eocene Thermal Maximum 2 (ETM-2) and the Paleocene-Eocene Thermal Maximum (PETM). Paleoceanogr. Paleoclimatol. 35. e2019PA003699.

Hauzer, H., Evans, D., Müller, W., Rosenthal, Y., Erez, J., 2018. Calibration of Na partitioning in the calcitic foraminifer *Operculina ammonoides* under variable Ca concentration: Toward reconstructing past seawater composition. Earth Planet. Sci. Lett. 497, 80–91.

Haynes, L.L., Hönisch, B., Dyez, K., Holland, K., Rosenthal, Y., Fish, C.R., Subhas, A.V., Rae, J.W.B., 2017. Calibration of the B/Ca proxy in the planktic foraminifer *Orbulina universa* to Paleocene seawater condition. Paleoceanography 32.

Haynes, L.L., Hönisch, B., Holland, K., Rosenthal, Y., Eggins, S.M., 2019. Evaluating the planktic foraminiferal B/Ca proxy for application to deep time paleoceanography. Earth Planet. Sci. Lett. 528, 115824.

Hellebrandt, S.E., Hofmann, S., Jordan, N., Barkleit, A., Schmidt, M., 2016. Incorporation of Eu(III) into calcite under recrystallization conditions. Sci. Rep. 6, 33137.

Hemming, N.G., Hanson, G.N., 1992. Boron isotopic composition and concentration in modern marine carbonates. Geochim. Cosmochim. Acta 56, 537–543.

Hemming, N.G., Reeder, R.J., Hanson, G.N., 1995. Mineral-fluid partitioning and isotopic fractionation of boron in synthetic calcium carbonate. Geochim. Cosmochim. Acta 59, 371–379.

Hemming, N.G., Reeder, R.J., Hart, S.R., 1998. Growth-step-selective incorporation of boron on the calcite surface. Geochim. Cosmochim. Acta 62, 2915–2922.

Henehan, M.J., Foster, G.L., Rae, J.W.B., Prentice, K.C., Erez, J., Bostock, H.C., Marshall, B.J., Wilson, P.A., 2015. Evaluating the utility of B/Ca ratios in planktic foraminifera as a proxy for the carbonate system: A case study of *Globigerinoides ruber*. Geochem. Geophys. Geosyst. 16.

Henehan, M.J., Gebbinck, C.D.K., Wyman, J.V.B., Hain, M.P., Rae, J.W.B., Hönisch, B., Foster, G.L., Kim, S.-T., 2022. No ion is an island: Multiple ions influence boron incorporation into $CaCO_3$. Geochim. Cosmochim. Acta 318, 510–530.

Hoffman, S., Voïtchovsky, K., Spijker, P., Schmidt, M., Stumpf, T., 2016. Visualising the molecular alteration of the calcite (104)-water interface by sodium nitrate. Sci. Rep. 6, 21576.

Holcomb, M., DeCarlo, T.M., Gaetani, G.A., McCulloch, M., 2016. Factors affecting B/Ca ratios in synthetic aragonite. Chem. Geol. 437, 67–76.

Horita, J., Zimmermann, H., Holland, H.D., 2002. Chemical evolution of seawater during the Phanerozoic: implications from the record of marine evaporites. Geochim. Cosmochim. Acta 66, 3733–3756.

Hönisch, B., Eggins, S.M., Haynes, L.L., Allen, K.A., Holland, K.D., Lorbacher, K., 2019. Boron Proxies in Paleoceanography and Paleoclimatology. Wiley-Blackwell, p. 248.

Ishikawa, M., Ichikuni, M., 1981. Coprecipitation of phosphate with calcite. Geochem. J. 15, 283–288.

Ishikawa, M., Ichikuni, M., 1984. Uptake of sodium and potassium by calcite. Chem. Geol. 42, 137–146.

Kaczmarek, K., Nehrke, G., Misra, S., Bijma, J., Elderfield, H., 2016. Investigating the effects of growth rate and temperature on the B/Ca ratio and $\delta^{11}B$ during inorganic calcite formation. Chem. Geol. 421, 81–92.

Kakihana, H., Kotaka, M., Satoh, S., Nomura, M., Okamoto, M., 1977. Fundamental studies on the ion-exchange of boron isotopes. Bull. Chem. Soc. J. 50, 158–163.

Katz, M.E., Cramer, B.S., Franzese, A., Hönisch, B., Miller, K.G., Rosenthal, Y., Wright, J. D., 2010. Traditional and emerging geochemical proxies in foraminifera. J. Foraminifer. Res. 40, 165–192.

Kester, D.R., Pytkowicz, R.M., 1969. Sodium, magnesium, and calcium sulfate ion-pairs in seawater at 25 °C. Limnol. Oceanogr. 14, 686–692.

Kitano, Y., Okumura, M., Idogaki, M., 1975. Incorporation of sodium, chloride and sulfate with calcium carbonate. Geochem. J. 9, 75–84.

Kitano, Y., Okumura, M., Idogaki, M., 1978. Uptake of phosphate ions by calcium carbonate. Geochem. J. 12, 29–37.

Klochko, K., Kaufman, A.J., Yao, W., Byrne, R.H., Tossell, J.A., 2006. Experimental measurement of boron isotope fractionation in seawater. Earth Planet. Sci. Lett. 248, 276–285.

Konrad, F., Gallien, F., Gerard, D.E., Dietzel, M., 2016. Transformation of amorphous calcium carbonate in air. Cryst. Growth Des. 16, 6310–6317.

Kontrec, J., Kralj, D., Brečević, L., Falini, G., Fermani, S., Noethig-Laslo, V., Mirosavljević, K., 2004. Incorporation of inorganic anions in calcite. Eur. J. Inorg. Chem., 4579–4585

Larsen, K., Bechgaard, K., Stipp, S.L.S., 2010. Modelling spiral growth at dislocations and determination of critical step lengths from pyramid geometries on calcite $\{10\bar{1}4\}$ surfaces. Geochim. Cosmochim. Acta 74, 558–567.

Lazić, S., 1995. Microcrystalline hydroxyapatite formation from alkaline solutions. J. Cryst. Growth 147, 147–154.

Lin, Y.-P., Singer, P.C., 2005. Inhibition of calcite crystal growth by polyphosphates. Water Res. 39, 4835–4843.

Lowenstein, T.K., Hardie, L.A., Timofeeff, M.N., 2003. Secular variation in seawater chemistry and the origin of calcium chloride basinal brines. Geology 31, 857–860.

Martin, R.I., Brown, P.W., 1997. Aqueous formation of hydroxyapatite. J. Biomed. Mater. Res. 35, 299–308.

Mason, H.E., Frisia, S., Tang, Y., Reeder, R.J., Phillips, B.L., 2007. Phosphorus speciation in calcite speleothems determined from solid-state NMR spectroscopy. Earth Planet. Sci. Lett. 254, 313–322.

Mavromatis, V., Montouillout, V., Noireaux, J., Gaillardet, J., Schott, J., 2015. Characterization of boron incorporation and speciation in calcite and aragonite from co-precipitation experiments under controlled pH, temperature and precipitation rate. Geochim. Cosmochim. Acta 150, 299–313.

Mavromatis, V., Purgstaller, B., Louvat, P., Faure, L., Montouillout, V., Gaillardet, J., Schott, J., 2021. Boron isotope fractionation during the formation of amorphous calcium carbonates and their transformation to Mg-calcite and aragonite. Geochim. Cosmochim. Acta 315, 152–171.

Mucci, A., Morse, J.W., 1983. The incorporation of Mg^{2+} and Sr^{2+} into calcite overgrowths: influences of growth rate and solution composition. Geochim. Cosmochim. Acta 47, 217–233.

Mucci, A., 1986. Growth kinetics and composition of magnesian calcite overgrowths precipitated from seawater: Quantitative influence of orthophosphate ions. Geochim. Cosmochim. Acta 50, 2255–2265.

Nielsen, M.R., Sand, K.K., Rdriguez-Blanco, J.D., Bovet, N., Generosi, J., Dalby, K.N., Stipp, S.L.S., 2016. Inhibition of calcite growth: Combined effects of Mg^{2+} and SO_4^{2-}. Cryst. Growth Des. 16, 6199–6207.

Nir, O., Vengosh, A., Harkness, J.S., Dwyer, G.S., Lahav, O., 2015. Direct measurement of the boron isotope fractionation factor: Reducing the uncertainty in reconstruction ocean paleo-pH. Earth Planet. Sci. Lett. 414, 1–5.

Noireaux, J., Mavromatis, V., Gaillardet, J., Schott, J., Montouillout, V., Louvat, P., Rollion-Bard, C., Neuville, D.R., 2015. Crystallographic control on the boron isotope paleo-pH proxy. Earth Planet. Sci. Lett. 430, 398–407.

Okumura, T., Kim, H.-J., Kim, J.-W., Kogure, T., 2018. Sulfate-containing calcite: crystallographic characterization of natural and synthetic materials. Eur. J. Mineral. 30, 929–937.

Paquette, J., Reeder, R.J., 1995. Relationship between surface structure, growth mechanism, and trace element incorporation in calcite. Geochim. Cosmochim. Acta 59, 735–749.

Parkhurst, D.L., Appelo, C.A.J., 2013. Description of Input and Examples for PHREEQC version 3—A Computer Program for Speciation, Batch-Reaction, One-Dimensional Transport, and Inverse Geochemical Calculations: U.S. Geological Survey Techniques and Methods. Book 6: p. 497 (http://pubs.usgs.gov/tm/06/a43/).

Penman, D.E., Hönisch, B., Zeebe, R.E., Thomas, E., Zachos, J.C., 2014. Rapid and sustained surface ocean acidification during the Paleocene-Eocene Thermal Maximum. Paleoceanog. 29, 357–369.

Plant, L.J., House, W.A., 2002. Precipitation of calcite in the presence of inorganic phosphate. Colloids Surf. A: Physicochem. Eng. Asp. 203, 143–153.

Plummer L.N., Parkhurst D.K., Fleming G.W., Dunkle S.A., 1988. A computer program incorporating Pitzer's equations for calculation of geochemical reactions in brines. U.S. Geological Society Water-Resources Investigations Report 88–4153, 310 p.

Quintana Krupinski, N.B., Russell, A.D., Pak, D.K., Paytan, A., 2017. Core-top calibration of B/Ca in Pacific Ocean *Neogloboquadrina incompta* and *Globigerina bulloides* as a surface water carbonate system proxy. Earth Planet. Sci. Lett. 466, 139–151.

Reeder, R.J., Lamble, G.L., Staudt, W.J., 1994. Mechanism of SeO_4^{2-} substitution in calcite: An XAFS study. Geochim. Cosmochim. Acta 58, 5639–5646.

Rimstidt, J.D., Balog, A., Webb, J., 1998. Distribution of trace elements between carbonate minerals and aqueous solutions. Geochim. Cosmochim. Acta 62, 1851–1863.

Ruiz-Agudo, E., Putnis, C.V., Kowacz, M., Ortega-Huertas, Putnis, A., 2012. Boron incorporation into calcite during growth: Implications for the use of boron in carbonates as a pH proxy. Earth Planet. Sci. Lett. 345–348, 9–17.

Saldi, G.D., Noireaux, J., Louvat, P., Faure, L., Balan, E., Schott, J., Gaillardet, J., 2018. Boron isotopic fractionation during adsorption by calcite – Implication for the seawater pH proxy. Geochim. Cosmochim. Acta 240, 255–273.

Salmon, K.H., Anand, P., Sexton, P.F., Conte, M., 2016. Calcification and growth processes in planktonic foraminifera complicate the use of B/Ca and U/Ca as carbonate chemistry proxies. Earth Planet. Sci. Lett. 449, 372–381.
Salter, M.A., Perry, C.T., Smith, A.M., 2019. Calcium carbonate production by fish in temperate marine environments. Limnol. Oceanogr. 64, 2755–2770.
Sanyal, A., Nugent, M., Reeder, R.J., Bijma, J., 2000. Seawater pH control on the boron isotopic composition of calcite: Evidence from inorganic calcite precipitation experiments. Geochim. Cosmochim. Acta 64, 1551–1555.
Shannon, R.T., 1976. Revised effective ionic radii and systematic studies of interatomic distances in halides and chalcogenides. Acta Crystallographica Section A 32, 751–767.
Song, J., Zeng, Y., Wang, L., Duan, X., Puerto, M., Chapman, W.G., Biswal, S.L., Hirasaki, G.J., 2017. Surface complexation modeling of calcite zeta potential measurements in brines with mixed potential determining ions (Ca^{2+}, CO_3^{2-}, Mg^{2+}, SO_4^{2-}) for characterizing carbonate wettability. J. Colloid Interface Sci. 506, 169–179.
Staudt, W.L., Reeder, R.J., Schoonen, A.A., 1994. Surface structural controls on compositional zoning of SO_4^{2-} and SeO_4^{2-} in synthetic calcite single crystals. Geochim. Cosmochim. Acta 58, 2087–2098.
Tang, Y., Elzinga, E.J., Lee, Y.J., Reeder, R.J., 2007. Coprecipitation of chromate with calcite: Batch experiments and X-ray adsorption spectroscopy. Geochim. Cosmochim. Acta 71, 1480–1493.
Uchikawa, J., Zeebe, R.E., 2013. No discernible effect of Mg^{2+} ions on the equilibrium oxygen isotope fractionation in the CO_2-H_2O system. Chem. Geol. 343, 1–11.
Uchikawa, J., Penman, D.E., Zachos, J.C., Zeebe, R.E., 2015. Experimental evidence for kinetic effects on B/Ca in synthetic calcite: Implications for potential $B(OH)_4$ and $B(OH)^3$ incorporation. Geochim. Cosmochim. Acta 150, 171–191.
Uchikawa, J., Harper, D.T., Penman, D.E., Zachos, J.C., Zeebe, R.E., 2017. Influence of solution chemistry on the boron content in inorganic calcite grown in artificial seawater. Geochim. Cosmochim. Acta 218, 291–307.
Vavouraki, A.I., Putnis, C.V., Putnis, A., Koutsoukos, P.G., 2008. An atomic force microscopy study of the growth of calcite in the presence of sodium sulfate. Chem Geol. 253, 243–251.
Wit, J.C., de Nooijer, L.J., Wolthers, M., Reichart, G.-J., 2013. A novel salinity proxy based on Na incorporation into foraminiferal calcite. Biogeosciences 10, 6375–6387.
Wynn, P.M., Fairchild, I.J., Borsato, A., Spötl, C., Hartland, A., Barker, A., Frisia, S., Baldini, J.U.L., 2018. Sulphate partitioning into calcite: Experimental verification of pH control and application to seasonality in speleothems. Geochim. Cosmochim. Acta 226, 69–83.
Yoshimura, T., Tamenori, Y., Suzuki, A., Kawahata, H., Iwasaki, N., Hasegawa, H., Nguyen, L.T., Kuroyanagi, A., Yamazaki, T., Kuroda, J., Ohkouchi, N., 2017. Altervalent substitution of sodium for calcium in biogenic calcite and aragonite. Geochim. Cosmochim. Acta 202, 21–38.
Zeebe, R.E., Sanyal, A., 2002. Comparison of two potential strategies of planktic foraminifera for house building: Mg^{2+} or H^+ removal? Geochim. Cosmochim. Acta 66, 1159–1169.
Zeebe, R.E., Tyrrell, T., 2019. History of carbonate ion concentration over the last 100 million years II: Revised calculations and new data. Geochim. Cosmochim. Acta 257, 373–392.
Zeebe, R.E., Wolf-Gladrow, D.A., 2001. CO_2 in seawater: equilibrium, kinetics, isotopes. Elsevier Oceanography Series, Amsterdam.
Zhang, P.M., Austad, T., 2006. Wettability and oil recovery from carbonates: effects of temperature and potential determining ions. Colloids Surf. A: Physicochem. Eng. Asp. 279, 179–187.
Zhang, D., Xu, H., Konishi, H., Roden, A.E., 2010. A relationship between d_{104} value and composition in the calcite-disordered dolomite solid-solution series. Am. Min. 95, 1650–1656.
Zhang, S., Henehan, M.J., Hull, P.M., Reid, P., Hardisty, D.S., vS Hood, A., Planavsky, N. J., 2017. Investigating controls on boron isotope ratios in shallow marine carbonates. Earth Planet. Sci. Lett. 458, 380–393.
Zhou, X., Rosenthal, Y., Haynes, L., Si, W., Evans, D., Huang, K.-F., Hönish, B., Erez, J., 2021. Planktic foraminiferal Na/Ca: A potential proxy for seawater calcium concentration. Geochim. Cosmochim. Acta 305, 306–322.
Zou, Z., Xie, J., Macías-Sánchez, E., Fu, Z., 2020. Nonclassical crystallization of amorphous calcium carbonate in the presence of phosphate ions. Cryst. Growth Des. 21, 414–423.